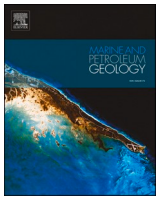
Marine and Petroleum Geology 163 (2024) 106741



Contents lists available at ScienceDirect

Marine and Petroleum Geology

journal homepage: www.elsevier.com/locate/marpetgeo



Mechanism of island dolostones formation in the Cretaceous calcitic ocean: Insights from the Mid-Pacific Guyots

Mahmoud Samir El-Yamani [a,b,*], Cédric M. John [a], Rebecca Bell [a]

[a] Department of Earth Science & Engineering, Faculty of Engineering, Royal School of Mines, Imperial College London, Prince Consort Road, South Kensington, SW7 2BP, UK

[b] Department of Geology, Faculty of Science, Ain Shams University, Cairo, 11566, Egypt

ARTICLE INFO

Keywords:
Seawater dolomite
Island dolomitization
Magmatic emplacement
Seismic interpretation
Dolomite geochemistry
Isolated carbonate platforms
Cretaceous
Hydrothermal dolomite

ABSTRACT

Dolomite is common in carbonate successions. There is an ongoing debate about the origin of ancient massive dolostones. Recent studies suggest widespread syndepositional and early-burial dolomitisation by normal and near-normal seawater, in the rock record, than previously recognised. Seawater dolomitisation is ubiquitous in Cenozoic islands but Cretaceous counterparts are rare, except for Resolution and Allison guyots, Mid-Pacific Mountains. We explored their dolomitisation conditions and the implications on our understanding of Cretaceous normal seawater syndepositional and near-surface dolomitisation. Integrating geochemical and borehole data reveals temporal overlap between $^{87}Sr/^{86}Sr$ ages of dolomites, and K/Ar and $^{40}Ar/^{39}Ar$ ages of the basement. Dolomites near basaltic basement exhibit 42-times Fe-enrichment compared to normal seawater dolomites. Host-rock thermal modelling suggested that $\delta^{18}O_{dol}$ temperatures are ~18–29 °C higher than concurrent temperatures. Seismic interpretation and seismic facies forward modelling demonstrate a spatial overlap between dolomites and magmatic sills in both guyots. Accordingly, magmatically driven hydrothermal dolomitisation is proposed, which promoted dolomitisation by providing high heat flow, increasing seawater circulation, and overcoming limited dolomitisation potential of Cretaceous seawater. The H_2O–CO_2–SO_2–HCl-rich magmatic-hydrothermal acidic fluids would mix with seawater causing slight modification by leaching Mg and Fe from basaltic basement. Consequently, magmatically active Cretaceous islands had greater potential for seawater dolomitisation than counterparts with ceased magmatism, due to increased heat flux and slight increase in Mg:Ca of dolomitising fluids. Our findings imply that deep-seated island dolostones don't only form by deep cold seawater below calcite saturation depth. Instead, magmatism appears crucial in this study and potentially other locations (e.g. Xisha Islands). The absence of dolostones in other Cretaceous islands supports previous models of reduced effectiveness of massive dolomitisation by Cretaceous normal seawater, questioning interpretations of syndepositional and near-surface dolomitisation. Thus, caution is advised when interpreting these dolomites by considering additional factors (dolomite geometry, geological settings, and dolomitisation age), as they may share characteristics with syndepositional and near-surface normal seawater dolomites.

1. Introduction

Dolomite ($CaMg(CO_3)_2$) is abundant in the rock record and scarce in modern sedimentary environments (e.g. Land, 1985). However, some challenge this view suggesting significant dolomite formation in the Neogene (e.g. Shalev et al., 2019). The origin of dolomite has been a puzzling topic for over two centuries, known as the "Dolomite Problem", due to the challenge of synthesising dolomite at laboratory conditions resembling the Earth's surface temperature (e.g. Gregg et al., 2015). Recent studies propose that early syndepositional dolomitisation by marine fluids (normal and near-normal) is more widespread than believed (Newport et al., 2017, 2020; Manche and Kaczmarek, 2019; Ryan et al., 2020), even in modern deep ocean sediments (e.g. Shalev et al., 2019). Seawater dolomites are ubiquitous in Cenozoic islands and atolls (e.g. Grand Cayman, Cayman Brac, Little Bahama Bank, Great Bahama Bank, Niue, Enewetak, Jamaica, and Kita-daito-jima, Schlanger et al., 1963; Land, 1973; Jones, 1989; Pleydell et al., 1990; Land, 1991; Whitaker et al., 1994; Vahrenkamp and Swart, 1994; Budd, 1997;

* Corresponding author. Department of Earth Science & Engineering, Faculty of Engineering, Royal School of Mines, Imperial College London, Prince Consort Road, South Kensington, SW7 2BP, UK.
E-mail address: mahmoud.elyamani19@imperial.ac.uk (M.S. El-Yamani).

https://doi.org/10.1016/j.marpetgeo.2024.106741
Received 22 September 2023; Received in revised form 30 January 2024; Accepted 31 January 2024
Available online 12 February 2024
0264-8172/© 2024 The Authors. Published by Elsevier Ltd. This is an open access article under the CC BY license (http://creativecommons.org/licenses/by/4.0/).

Wheeler et al., 1999; Jones et al., 2001; Jones and Luth, 2002; Melim et al., 2002; MacNeil and Jones, 2003; Jones, 2005; Suzuki et al., 2006; Zhao and Jones, 2012a, b). These dolomites were formed from unmodified seawater (Warren, 2000; his Fig. 10) via deep cold seawater pumping below calcite saturation depth (e.g. Enewetak atoll deep-seated dolomites; Saller, 1984), reflux of slightly concentrated seawater (e.g. Machel and Burton, 1994; Wang et al., 2022), tidal pumping (e.g. Carballo et al., 1987), and Kohout convection (e.g. Aharon et al., 1987; Wheeler et al., 1999; Swart and Melim, 2000). Approximately 80% of Cenozoic islands and atolls yield dolostones from normal seawater origin, while ~40% of Cretaceous islands and atolls are dolomitised with ~11% of them were suggested to be from normal seawater origin (Fig. 1; check Supplemental Sheet T1 and T2 for the criteria of compiling and analysing the geo-dataset of drilled and/or

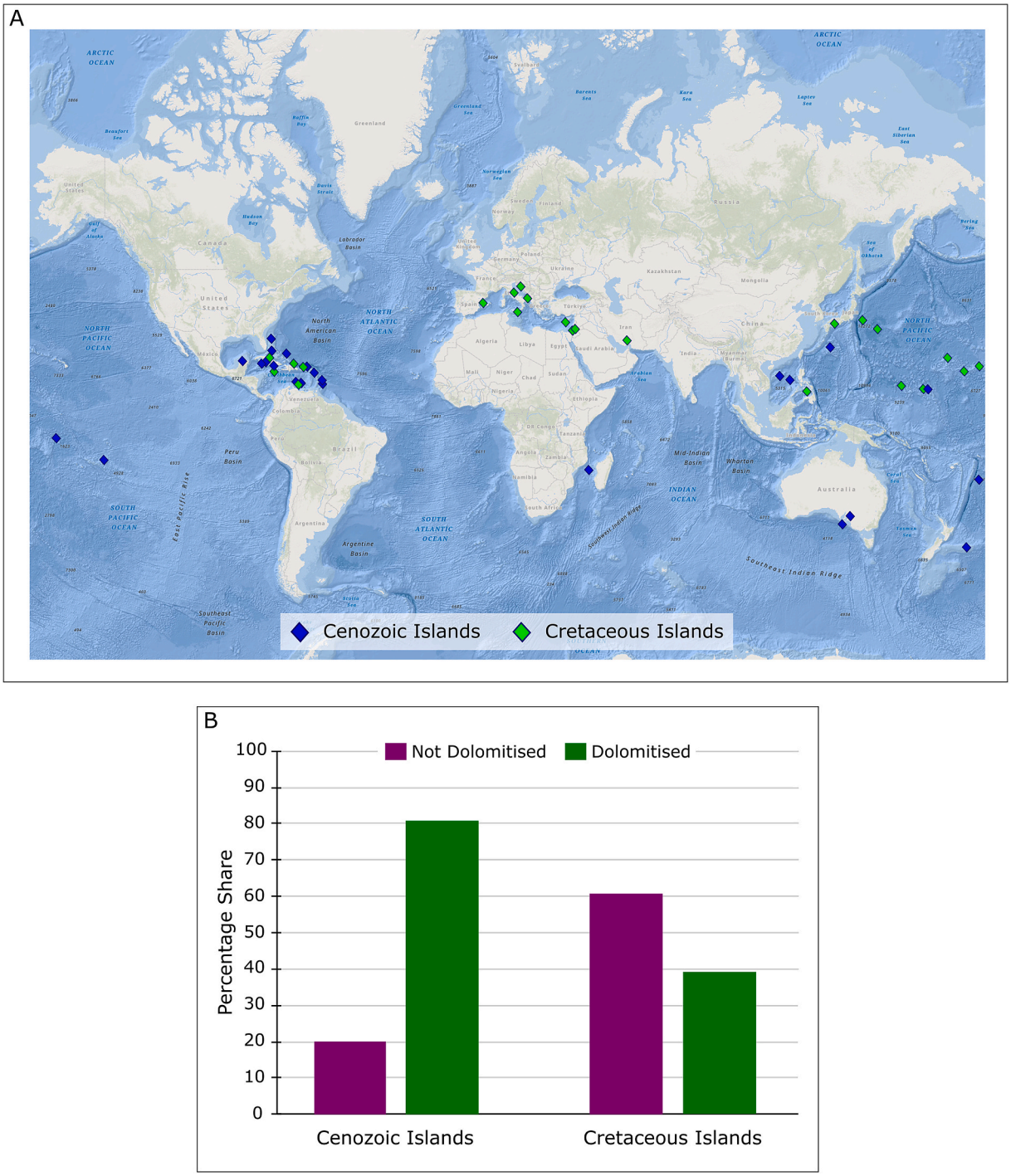


Fig. 1. The compiled geo-dataset of Cenozoic and Cretaceous islands and atolls (see Supplemental Sheets T1 and T2). (A) World map of the distribution of the Cretaceous and the Cenozoic carbonate islands and atolls. (B) The percentage of dolomitised and not dolomitised carbonate islands and atolls of the Cretaceous and the Cenozoic ages. The compiled dataset might not be quantitatively representative of all the formed islands and atolls in the earth during the Cretaceous and the Cenozoic as not all of them were drilled or are outcropping. Therefore, the presented dataset might not represent a complete rock record. Although, it can provide, at least, a source of a relative comparison to show the difficulty of unmodified seawater dolomitisation in the Cretaceous islands in comparison with the Late Cenozoic islands and atolls.

outcropped Cenozoic and Cretaceous carbonate islands and atolls).

Most Cenozoic islands were dolomitised during the Late Miocene to Late Pleistocene (~10–0.5 Ma; Wang et al., 2019) when Cenozoic aragonitic seawater (Fig. 2) had high Mg^{2+} concentrations (~49–55.1 mmol) and Mg:Ca (~5.2) and were highly supersaturated with respect to dolomite (Brennan et al., 2013). In stark contrast, Cretaceous calcitic seawater (Fig. 2; Horita et al., 2002; Timofeeff et al., 2006) had lower Mg^{2+} concentrations (30–42 mmol) and Mg:Ca (0.6–1.3). Consequently, dolomite saturation was lower than during the Late Cenozoic (e.g. Arvidson et al., 2011). These conditions favoured calcite precipitation over aragonite or high Mg-calcite which might have impacted dolomitisation potential of seawater (Steuber and Rauch, 2005) and likely hindered large-scale dolomitisation (e.g. Newport et al., 2017, 2020). In line with this, Gabellone and Whitaker (2016) using reactive transport modelling showed very limited dolomitisation potential and very low dolomitisation rates of normal Aptian seawater (~1–2% dolomite fraction), in contrast to modern seawater (~62% dolomite after 500 kyr). Despite the above, two notable exceptions to the scarcity of Cretaceous island dolostones, in the Pacific Cretaceous atolls, are Resolution and Allison guyots, both drowned atolls on volcanic basement (Figs. 3 and 4; Sager et al., 1993a, b). In both guyots, Sager et al. (1993b) and Strasser et al. (1995) suggested early syndepositional dolomitisation in intertidal and subtidal facies by seasonally evaporative pumping. In Resolution Guyot, Flood and Chivas (1995) suggested that the thick dolomitic limestone and dolostones were formed by normal seawater dolomitisation through deep cold seawater pumping at depths below calcite saturation depth by Kohout convection (e.g. Enewetak atoll; Saller, 1984).

In light of the above, this paper investigates dolomitisation conditions in Cretaceous islands and atolls, Resolution and Allison guyots, compared to Late Cenozoic counterparts to (a) understand the reasons behind the scarcity of dolostones in Cretaceous islands, (b) evaluate the effectiveness of syndepositional and near-surface early-burial dolomitisation by Cretaceous calcitic seawater, (c) emphasise the importance of distinguishing true syndepositional and near-surface early-burial normal seawater dolomites from other types of dolomites. Hence, the study (a) integrated seismic interpretation and seismic facies forward modelling, (b) utilised published geochemical and stable isotope data of dolomite, limestone, and basement from the Ocean Drilling Program (ODP), and (c) conducted burial and thermal modelling of the limestone host rock, in order to fully evaluate the controls on dolomitisation.

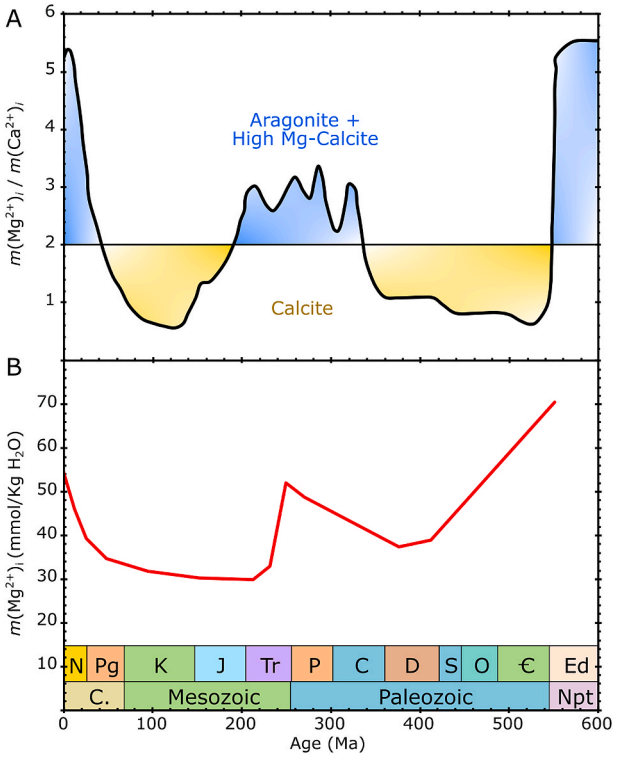


Fig. 2. Secular variations in molar Mg/Ca ratio (A) and Mg^{2+} concentration (B) in seawater throughout the Phanerozoic (Hardie, 1996; Horita et al., 2002; Demicco et al., 2005).

2. Geological settings

This study focuses on Resolution and Allison guyots which are parts of the Mid-Pacific Mountains, a volcanic plateau formed within the region of intense hotspot volcanism known as the South Pacific isotopic and thermal anomaly (Fig. 3; Staudigel et al., 1991). It is characterised by flat-topped seamounts with shallow marine limestone cover and pelagic cap, including Sio, Heezen, Resolution, Jacqueline, Allison, Cape Johnson, Renard, and Horizon atolls (Winterer and Sager, 1995). These were targeted with other Mesozoic Pacific Guyots by ODP Leg 143/144 and Roundabout Expedition Leg 10 cruise. Resolution (Site 866) and Allison (Site 865) guyots have a ~570-600 m thick unit of dolostone and dolomitic limestone on top of basaltic basement and a ~180 m thick unit of clayey dolomitic limestone sitting on top of drilled magmatic sills, respectively (Figs. 3 and 4; Sager et al., 1993a, 1993b). At Allison Guyot, early diagenetic dolomite occurrences are documented in some layers between 660 and 837 metres below seafloor (mbsf) at Site 865 (Sager et al., 1993b). Burrows exhibit preferential dolomitisation owing to their higher permeability (Sager et al., 1993b). XRD analysis by Murdmaa et al. (1995) between 670-836 mbsf reveals varying degrees of dolomite abundance, ranging from abundant to rare. Dolomite occurrences within Resolution Guyot are notable, commencing at ~500 mbsf and recurring ~900 mbsf (Sager et al., 1993a). Further downhole, dolomite persists continuously below ~1000 mbsf, with brown dolomite prevalent in sediments from ~1200 to ~1620 mbsf in lithostratigraphic Units VII and VIII (Site 866; Flood and Chivas, 1995). The dolomitised succession at Site 866 contains a distinct white dolomite interval spanning 30 m (1250–1280 mbsf; Flood, 1998) within the broader brown dolomite context. This white dolomite interval exhibits a markedly different $^{87}Sr/^{86}Sr$ ratio of 0.70822, consistent with an Oligo-Miocene age, contrasting with the $^{87}Sr/^{86}Sr$ of the surrounding brown dolomites of ~0.70735, which aligns with the Cretaceous Age (Flood and Chivas, 1995; Flood et al., 1996; Flood, 1998). Given the focus of the paper on Cretaceous island dolomitisation, we exclude the 30-m interval of the Cenozoic white dolomite from our analyses. In both guyots, Resolution and Allison, an active exchange between pore-waters and surrounding modern seawater is evident based on similar $^{87}Sr/^{86}Sr$, major-element composition, and $\delta^{18}O$ (Sager et al., 1993a, 1993b; Paull et al., 1995; Flood, 1998) indicating that open ocean water freely circulates through the islands.

3. Data & methods

This paper utilises core-log-seismic data collected during ODP Leg 143/144 and the Roundabout Expedition Leg 10 at Resolution and Allison guyots. Seismic data (Fig. 3) were collected by cruise 'Roundabout Expedition Leg 10' (RNDB10WT; Nov–Dec 1988) aboard the R/V Thomas Washington which was a dedicated program to image the Mesozoic Guyots in the western Pacific. This survey consisted of single-channel, 2D seismic profiles acquired using an 80-in^3 water gun, processed by the University of Texas Institute for Geophysics. Processing involved filtering (50–200), mixing (1:1:1), and automatic gain control (Marine Geoscience Data System, n.d.). This study used wireline-logging data including sonic (DTLN), formation density (RHOB), photoelectric absorption factor (PEF), and neutron porosity (NPHI) (Division of Marine and Large Program, n. d.; Supplemental Sheet T3). High-resolution core images were accessed from the International Ocean Discovery Program JOIDES Resolution Science Operator website (JOIDES

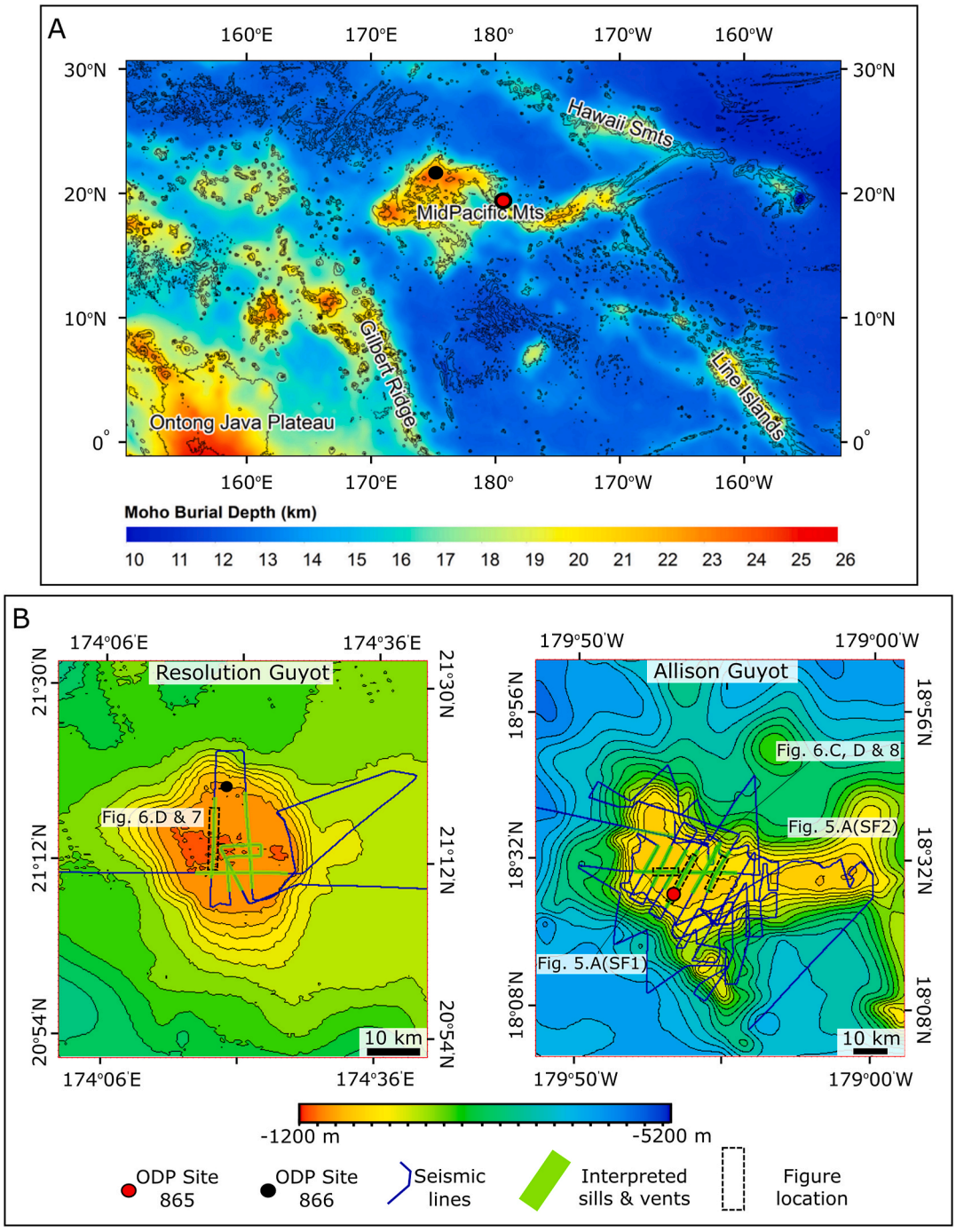


Fig. 3. A. The Pacific Ocean map showing the location of the Mid-Pacific Mountains and Resolution and Allison guyots (Bai et al., 2019). B. Bathymetry maps of Resolution and Allison guyots (Keizer et al., 2001) showing the locations of drilling sites 865 and 866 and the 2D seismic data.

Resolution Science Operator, n.d.). The geochemical aspects of this study are based on doing our own interpretations of the geochemical data that were generated by the Ocean Drilling Program in the Proceedings of the Scientific Results of Leg 143. This geochemical data encompasses Mn, Sr, and Fe content, $\delta^{18}O$, $\delta^{13}C$, and $^{87}Sr/^{86}Sr$ isotopes, and major, minor, and trace elements of dolostone and limestone at Site 866 and radiometric age data of basaltic basements in Leg 143 (Baker et al., 1995; Flood and Chivas, 1995; Jenkyns, 1995; Jenkyns et al., 1995; Pringle and Duncan, 1995; Sager, 1995; Röhl and Strasser, 1995; Supplemental Sheets T4-6). Table 1 summarises depth intervals of samples, standard sample, laboratory, device, techniques, data source, and corresponding supplemental sheet displaying the geochemical data values. Resolution Guyot offers a comprehensive dataset of geochemical, seismic reflection, and wireline-logging data, while Allison Guyot provides seismic reflection and wireline-logging data. Our analysis primarily focuses on Resolution Guyot but includes comparisons with Allison Guyot whenever data permits.

Constraining the spatial geological settings around the dolomites in the tied wells of Resolution and Allison guyots was achieved through doing seismic interpretation on the processed seismic data (as processed by University of Texas Institute for Geophysics). Seismic reflection datasets were interpreted and visualised using Petrel® software. The seismic data is displayed in the American polarity convention, where a downward increase in acoustic impedance (e.g. seabed) is represented

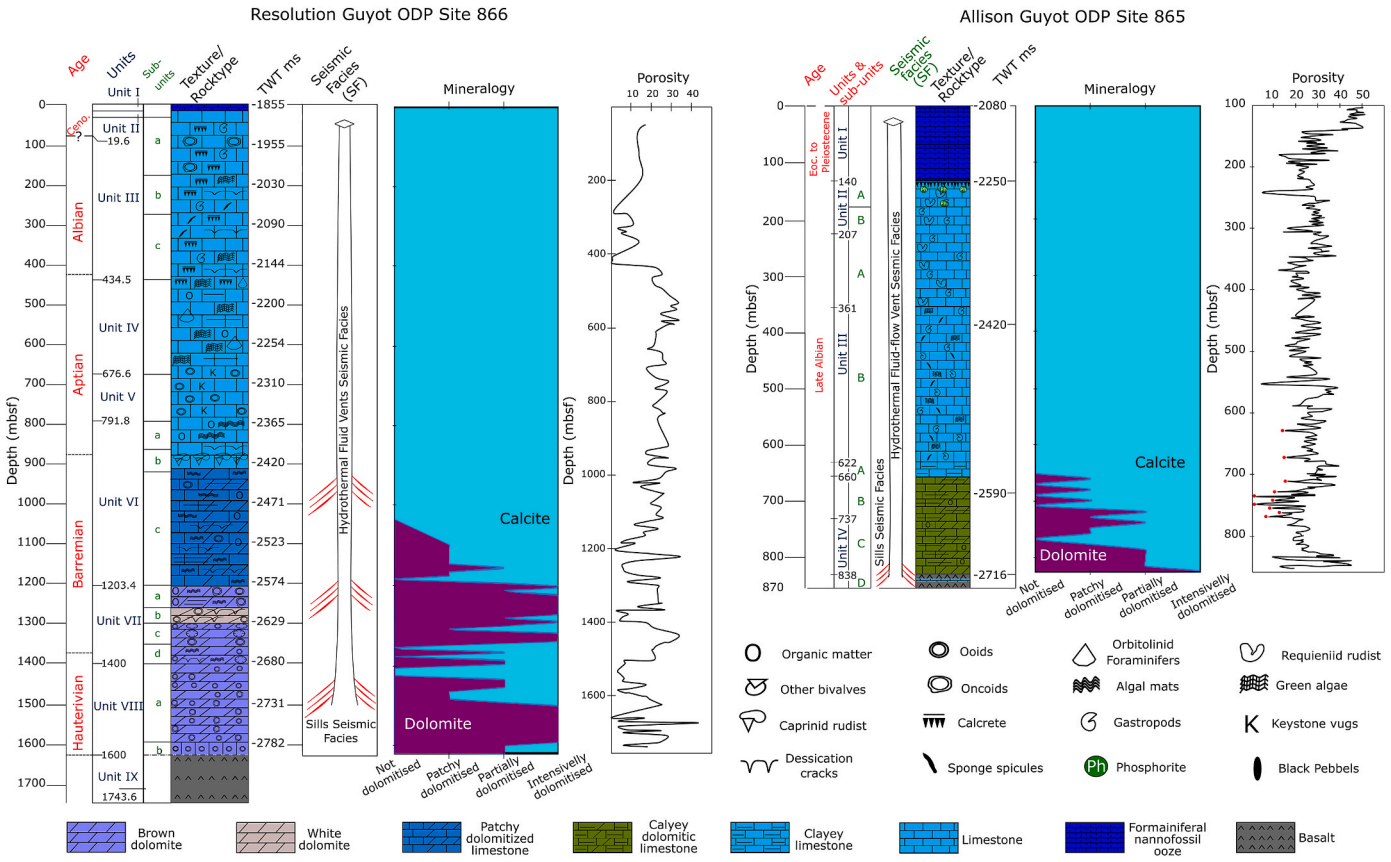


Fig. 4. Lithostratigraphic descriptions of Resolution (Site 866) and Allison (Site 865) guyots adapted from (Sager et al., 1993a, 1993b; El-Yamani et al., 2022). The figure shows a summary of the lithological and fossil content of the different lithostratigraphic units, and their porosity measurements (Sager et al., 1993a, 1993b) at different drill sites along with the identified seismic facies. The mineralogy profile of each drilling site was retrieved by integrating core scans, core descriptions (ODP Initial Reports, 1993a, 1993b), facies and petrographic descriptions (Arnaud et al., 1995). The red dots in the porosity profile of 865 represents the location of the identified dense beds that act as permeability barriers.

by trough-peak-trough with red-blue-red reflections. Seismic to well tie at sites 865 and 866 was performed using the time-depth relation of El-Yamani et al. (2022; Supplemental Sheet T7) and Sager et al. (1993b). Seismic facies and their corresponding depths and palaeogeographic distributions in atolls were categorised by interpreting reflection internal configuration and geometries, distribution of seismic reflections, and their signal properties (continuity, frequency, and amplitude; Mitchum et al., 1977). The interpreted seismic facies were constrained through making a 1D convolution forward seismic modelling where drilling data were available in one guyot and missing in the other, using RokDoc® software. Synthetic seismic facies forward modelling requires five inputs which are (a) a conceptual geologic model, (b) bulk densities ρ and compressional wave velocities V_p of the rock units in the conceptual model, (c) simulating a zero-offset survey using the Zoeppritz equations, (d) a zero-phase Ricker wavelet, (e) wavelet frequency (Magee et al., 2015). A suitable conceptual model to the seismic facies was built using the core descriptions (i.e. defining the different rock units and their thicknesses) and ρ and V_p of each rock unit. These petrophysical properties (ρ and V_p) were extracted from the wireline-logging data and the physical properties measurements (Sager et al., 1993a, 1993b). Wireline-log interpretation was performed using Interactive Petrophysics® software. The wavelet frequencies were extracted from the seismic data using dominant frequency attribute and the spectral analysis tool using Petrel® software.

One hundred and eleven thin sections, across the whole sedimentary section at Site 866, were utilised in this study on the dolomite from Resolution Guyot. Optical and cathodoluminescence microscopes at Imperial College London were used for analysis. Thin sections were studied using a transmitted light Zeiss Axioskop 40 with an AxioCam ICc1 camera. Cathodoluminescence (CL) microscopy was conducted on a Nikon Eclipse 50i luminoscope equipped with a CITL cathodoluminescence MK5-2 stage and an AxioCam ICc1 camera. The CL microscope operated at a current of 315 μA, an accelerating voltage of 15 kV, and a vacuum of 0.003 mBar. Dolomite crystal textures were described based on the classifications of Flügel (2010) and Gregg 1987. While crystal sizes were defined according to the classification of Chatalov (1971) and James and Jones (2015). Cathodoluminescence crystal zonation were described using the classification of Machel and Burton (1991). The occurrence of dolomite at Resolution Guyot was identified by integrating core images, MgO% plot, grain density plot, and RHOB, NPHI, and PEF wireline-logs due to the low core recovery (15% average) which were all checked with core descriptions and thin sections (Supplemental Sheet T8). Qualitative lithological interpretation from wireline-logs was based on (a) defining a dolomite dominated interval where PEF is 3.14–4.11 b/e and limestone dominated interval where PEF is > 4.11–5 b/e (Glover, 2000; Wang et al., 2015; Szabó et al., 2023) and (b) defining a dolomite dominated interval where RHOB is positively separated from PEF and vice versa for limestone dominated intervals (Wang et al., 2015). The grain density of samples from Site 866 (Sager et al., 1993a; Kenter and Ivanov, 1995) was used as a proxy for mineralogy (Zenger, 1968; Kenter and Ivanov, 1995) using the following equation.

$$\%dol = \frac{\rho_{sample} - \rho_{calcite}}{0.148} \times 100$$

where ρ_{sample} is the grain density of the sample considering grain

Table 1
Summary table of all the geochemical data used in this paper. The table shows types of data, number of samples, depths of samples, the techniques used and the laboratories, data source, standard samples, and the corresponding Supplemental Sheet of the data.

Rock Type	Geochemical Analysis	Number of Samples	Depth Ranges (mbsf)	Techniques & Laboratory	Data Sources	Standard Samples	Corresponding Supplemental Sheet of the Data
Dolostone	Sr isotope	9	1572–1224	Finnigan MAT 261 multicollector mass spectrometer at the Precise Radiogenic Isotope Services, Australian National University, Canberra	Flood and Chivas (1995)	SRM 987 and EN-1	T4
	$\delta^{18}O$	9	1572–1224	Isotopic measurements were performed at the Research School of Earth Sciences, Canberra	Flood and Chivas (1995)	NBS-18 and NBS-19	
	$\delta^{13}C$	9	1572–1224				
	Elemental analysis (Fe & Mn)	12	1611–1175	Microprobe analyses inductively coupled plasma atomic emission spectroscopy, Queensland University of Technology, Brisbane atomic. Microprobe analyses with absorption analysis by a Philips PU 9400X and inductively coupled plasma spectrometry by a sequential spectrometer Philips PU 7000.	Flood and Chivas (1995) & Röhl and Strasser (1995)		T5
	Elemental analysis (Sr)	6	1593–1252				
Limestone	Sr isotope	86	48–1611	VG Sector 54 thermal ionization mass spectrometer (TIMS) at the Department of Geology, University of North Carolina at Chapel Hill.	Jenkyns (1995) & Jenkyns et al. (1995)	NBS 987	T10
	$\delta^{18}O$	86	48–1611	VG Isocarb device and Prism mass spectrometer at Oxford University		NBS 19 and Cambridge Carrara marble	
	$\delta^{13}C$	86	48–1611				
	Elemental analysis (Fe & Mn)	13	10–1593	Microprobe analyses with absorption analysis by a Philips PU 9400X and inductively coupled plasma spectrometry by a sequential spectrometer Philips PU 7000.	Röhl and Strasser (1995)		T5
	Elemental analysis (Sr)	18	10–1593				
Bulk chemistry of the whole sedimentary succession		77	1591–39	X-ray-fluorescence analysis	Röhl and Strasser (1995)		T6

densities for calcite and dolomite are 2.71 and 2.87 gm/cm^3, respectively (Carmichael, 1989).

We utilise Fe, Sr, and Mn concentrations in dolomites to trace their potential sources in the dolomitising fluids (Budd, 1997). Dolomite age constraints at Site 866 were established by correlating dolomites' $^{87}Sr/^{86}Sr$ data with the Phanerozoic $^{87}Sr/^{86}Sr$ seawater compositions using LOWESS LOOK-UP TABLE 5B regressions (McArthur et al., 2012; check Supplemental Material S1). Calculating temperatures of the dolomitisation fluids at Site 866 involved employing Horita's (2014) oxygen isotope fractionation equation, dolomites' $\delta^{18}O_{dol}$, and a $\delta^{18}O_{sw}$ value of Mid-Cretaceous seawater (~0.2‰ VSMOW, the Mid-Cretaceous zonal $\delta^{18}O_{sw}$ at the guyots' paleogeographic location; Zhou et al., 2008; check Supplemental Sheet T9 for the corresponding $\delta^{18}O_{sw}$). Detailed calculation steps and results are discussed in Supplemental Material S2. Burial and thermal modelling aimed to reconstruct the concurrent host-rock temperatures during dolomitisation periods (detailed calculation steps and results are discussed in Supplemental Material S3). This involved integrating (a) depositional age model at Site 866 by El-Yamani et al. (2022) to reconstruct stratigraphic accumulation over time (Supplemental Sheet T10), (b) the new dolomitisation age model from this study, (c) the average sea surface temperature during Mid-Cretaceous (~33 °C) at the guyots' paleogeographic locations (using Scotese and Wright's, 2018 palaeogeographic reconstruction and Valdes's et al., 2021 palaeoclimatic simulations; detailed maps of the ocean surface temperatures are provided in Supplemental Sheet T9), and (d) geothermal gradient. Geothermal gradients in atolls and carbonate islands differ from continental areas as they have a negative gradient due to the active exchange between pore-water and surrounding seawater. Therefore, pore-water temperature profiles in carbonate islands and atolls should mimic those of the open marine profile (Warren, 2000). Instances from various locations such as Enewetak, Bikini, Kita-daito-jima, Fangataufa, Mururoa atolls, Reed Bank, Tahiti, Grand Cayman Islands, Florida Platform, and Yucatán Peninsula have been documented, showcasing gradients ranging from −2.2 °C/100 m in Reed bank and Mururoa atoll (Rougerie and Wauthy, 1993; Guille, 1996; Henry et al., 1996; Wang et al., 2020) to −2.5 to −3.2 °C/100 m in Mururoa atoll and Grand Cayman Island (Ren and Jones, 2017) up to −4.6 °C/100 in Tahiti Island (Steinmann and Déjardin, 2004). Considering the similarity in the dimensions and thickness of sedimentary cover between Enewetak atoll and Resolution guyot, the geothermal gradient of Enewetak atoll was employed (Swartz, 1958; detailed ranges are provided in Supplemental Sheet T11). Additionally, concentrations of major, minor, and trace elements at Site 866 were integrated with wireline-logging data (DTLN, RHOB, and NPHI). Frequency analysis and histograms were conducted on the wireline-logging data.

4. Results and interpretation

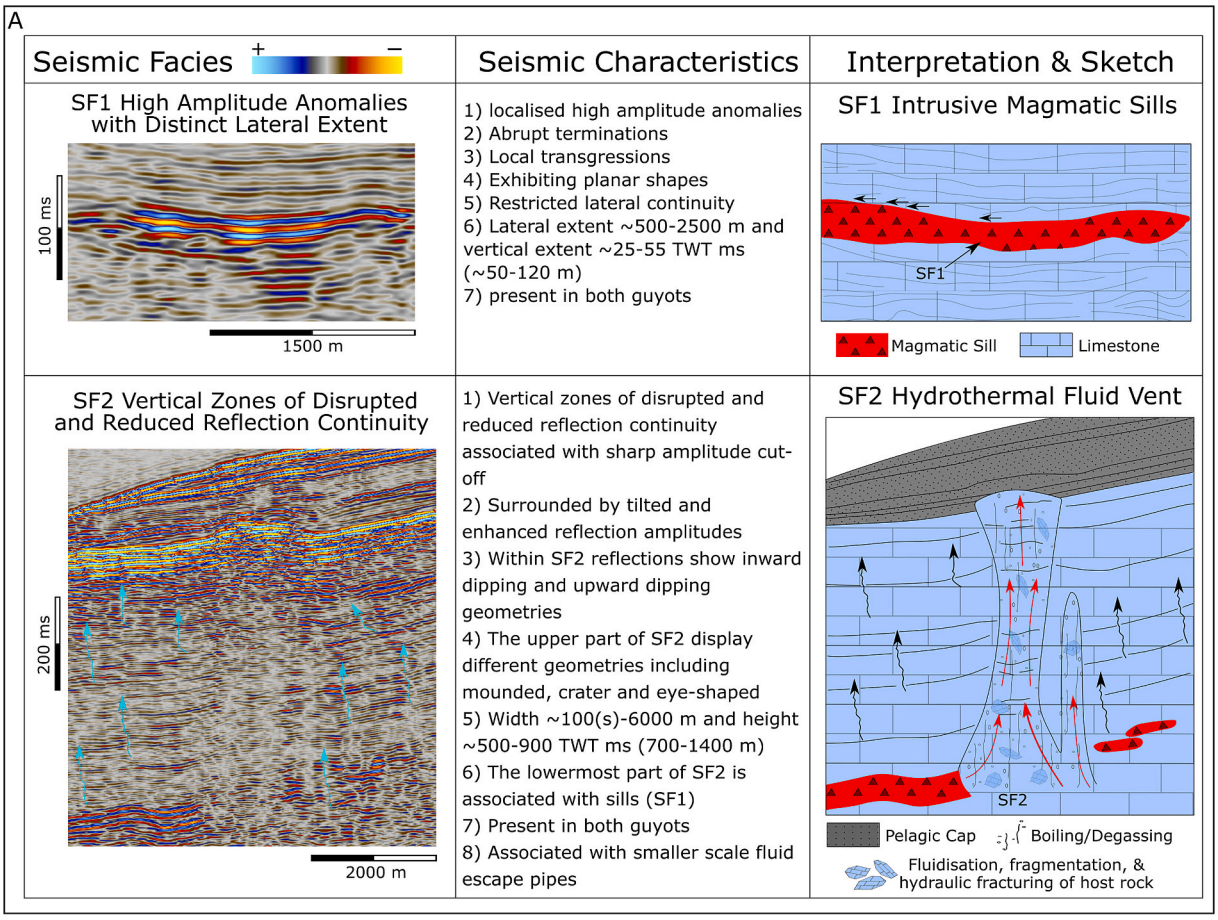
4.1. Seismic interpretation and seismic facies forward modelling

Seismic facies and their corresponding depths and palaeogeographic distributions in the atolls were categorised by analysing seismic properties like reflection pattern, continuity, amplitude, and internal and external geometry. Detailed characteristics of these seismic facies are explained with integrating drilling and wireline-logging data and comparing them with examples from high-resolution seismic data sets.

Seismic Facies 1 (SF1; Fig. 5): It displays a distinct seismic stratigraphic expression within the host-rock strata as it comprises localised, anomalous, high-amplitude, parallel reflections with limited lateral continuity and abrupt terminations. SF1 exhibits a sheet-like shape with predominantly concordant to locally crosscut relationships within the host-rock strata. At Resolution Guyot, SF1 is found between depths of −2725 and −2400 TWT-ms (two-way time millisecond; ~900–1500 mbsf), while at Allison Guyot, SF1 occurs at depths of −2775 to −2600 TWT-ms (~650->870 mbsf).

Interpretation

The seismic features of SF1 (i.e. high amplitude, concordant to locally crosscut relationships within the host-rock strata, sheet-like



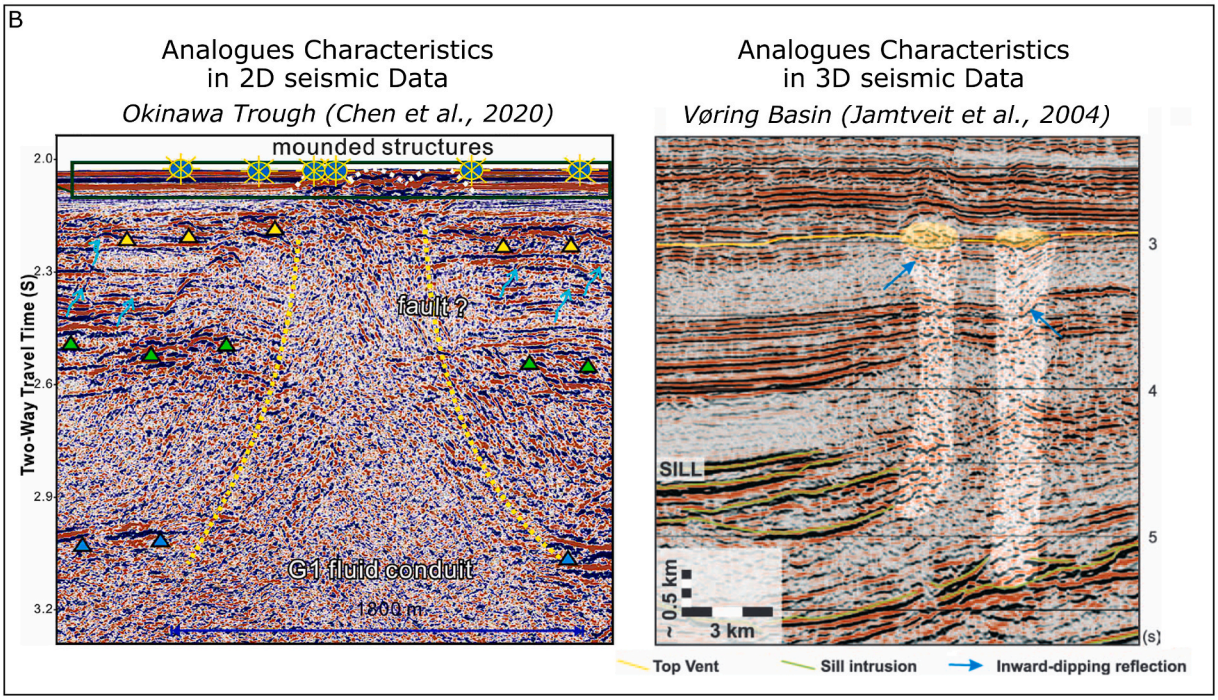


Fig. 5. A. The interpreted seismic facies at Resolution and Allison guyots showing an example of each seismic facies, summaries of their characteristics, and interpretation sketch of seismic facies. B. The Figure also show analogues seismic profiles with similar seismic facies from Okinawa Trough 2D seismic data (Chen et al., 2020) and Vøring Basin 3D seismic data (Jamtveit et al., 2004) to provide a source of comparison with the displayed characteristics of the seismic facies at the guyots.

shape, and abrupt terminations) closely resemble magmatic sill-intrusions observed in various 2D and 3D seismic data across different geological settings (Planke et al., 2000, 2005; Magee et al., 2015; Chen et al., 2020; Niyazi et al., 2021, Fig. 5). At Resolution Guyot, Site 866 did not encounter any drilled magmatic sill intruding through the sedimentary succession. Conversely, at Allison Guyot (Site 865), magmatic sill-intrusions penetrating limestones were found between depths of 830–871 mbsf. To validate our interpretation of SF1, seismic facies forward modelling was conducted. Utilising the drilling report from Allison Guyot (Sager et al., 1993b), detailing the thicknesses of drilled sills and the limestone they intruded, an input model was created (Fig. 6A). The drilling reports indicated compressional wave velocity and density of drilled sills at 4854 m/s and 2.7 kg/m^3, and for limestones, 3406 m/s and 2.4 kg/m^3, respectively. Dominant frequency attribute and spectral analysis tools revealed the seismic data's dominant frequency at both atolls to be ~65–75 Hz (Fig. 6B-C). The input model was transformed into synthetic seismic facies forward model by simulating a zero-offset survey using Zoeppritz equations and a zero-phase Ricker wavelet (Magee et al., 2015). The resulting seismic facies forward modelling demonstrated that the thickness and stacking pattern of magmatic sill-intrusions at Allison Guyot would produce six alternating troughs and peaks, characterised by localised, abrupt brightening of high amplitude reflections (Fig. 6D). This aligned with observations within the area of drilled sills at Allison Guyot and the seismic characteristics of interpreted bright reflection packages in Resolution Guyot (Fig. 6D). Consequently, we interpret SF1 as magmatic sills-intrusion intruding through sedimentary succession of Resolution Guyot between depths of −2700 to −2400 TWT ms (~900–1500 mbsf; Figs. 3 and 6. D) and Allison Guyot between depths of −2775 to −2600 TWT-ms (~650->870 mbsf).

Seismic Facies 2 (SF2; Fig. 5): The interpreted magmatic sill-intrusions in both guyots are associated with vertical zones of disrupted and reduced reflection continuity which are surrounded by tilted and enhanced reflection amplitudes. SF2 bases consistently align with the tips of interpreted magmatic sill-intrusions (Fig. 5). The upper part of SF2 exhibits eye-, crater-, mounded-, or dome-shaped geometry with a width of ~700-1700 m. The vertical disrupted zones of SF2 have inward-dipping reflections. Variance attribute highlights SF2 as zones of dim to chaotic reflections relative to the well-bedded reflections of the host-rock strata. Adjacent to SF2, localised areas show small-scale chaotic reflections and vertical discontinuities.

Interpretation

The interpreted seismic characteristics of SF2 (i.e. eye-, crater-, mounded-, or dome-shaped geometry of their upper parts, upward bending of surrounding seismic reflections, disrupted reflections within SF2, their inward-dipping reflections, and their intimate association with underlying magmatic sill-intrusion) strongly resemble hydrothermal vent complexes associated with magmatic intrusions as identified in 2D and 3D seismic data across various geological settings (Jamtveit et al., 2004; Planke et al., 2005; Chen et al., 2020, Fig. 5). The smaller-scale zones of chaotic reflections and vertical discontinuities surrounding SF2 (Figs. 5, 7 and 8) are interpreted as fluid escape pipes (Huang et al., 2020). SF2 spans a width of 300–1500 m in both guyots, up to 5000–6000 m at their centres (Figs. 7 and 8). The interpreted sills and associated hydrothermal vents extend across both guyots' widths (Fig. 3) but are primarily concentrated in the middle. The horizontal distance of the closest hydrothermal vents complexes to the dolomites at Resolution and Allison guyots drilling sites is ~2600 to 2000 m, respectively.

4.2. Dolostone core and petrographic observations

4.2.1. Macroscale dolostone textures

The sedimentary sequence at Resolution Guyot comprises non-dolomitised limestones, partially/patchy dolomitised limestones, and dolostones (Fig. 9). Dolostones are distinguished by their dark brown colour (Fig. 9G, H) compared to the beige, cream, and light brown hues of limestone and dolomitic limestone (Fig. 9A-F). Identifying dolomite at Resolution Guyot involved integrating core images, MgO% and grain density plots, and wireline-logs due to low core recovery. The integrated approach delineates (Fig. 10): (a) complete dolomitisation at 1620-1500 mbsf, (b) intervals partially dolomitised alternating with limestones at 1500-1360 mbsf, (c) partially to completely dolomitised succession at 1360-1160 mbsf, (d) patchy dolostones intercalating with limestones above 1160 and below 1000 mbsf. Dolomite is almost absent in cores, thin sections, and seamer slides descriptions above this level (ODP Initial Reports, 1993a) which suggest that the interpreted intervals in wireline-logs above that are mistakenly identified possibly due to (a) the bad conditions of the borehole (note wireline-logs spikiness; check Supplemental Sheet T8), and (b) presences of clays in the limestone which can have overlapping densities (2.6–3.3 gm/cm^3; Deer et al., 1966) with dolomite.

In pervasively dolomitised sections, fine to medium crystalline dark brown replacive dolomite matrix exists, with molds and vugs filled by medium to coarse crystalline golden-light brown dolomite cements (Fig. 9G, H). Precursor limestone fabrics are mostly well preserved, showing carbonate grains and mouldic pores (Fig. 9G, H). The calcitic carbonate grains (e.g. ooids, oncoids, pisoids, bivalves) show different preservation levels from unaltered to partially or totally dolomitised (Fig. 9G, H). Partially and patchy dolomitised sections display lighter brown to cream colours, with mainly fine to medium crystalline replacive dolomite, replacing matrix and grains (Fig. 9B-D, F).

4.2.2. Microscale dolomite textures

Replacive dolomites (RD) show finely to medium crystalline (100–300 μm) planar-e and planar-s textures (Fig. 11). The Pervasively dolomitised sections have a densely interlocked mosaic (Fig. 11A-C), while partially to patchy dolomitised sections are less dense (Fig. 11D-F). Dolomite cements (DC) are present throughout the whole section with finely to medium crystalline (150–350 μm up to 400–500 μm) planar-s to non-planar textures (Fig. 11). Dolomite cements partially to fully occlude mouldic, vuggy, interparticle and intercrystalline porosities (Fig. 11F). In some cases, dolomite cements have finer crystals lining vugs and coarser crystals in the centre. Original limestone fabrics are mostly preserved with varying degrees from totally to partially retentive to ghost structures of preexisting carbonate grains (e.g. ooid, peloids, oncoids, bioclasts; Fig. 11A-C, E). In few cases, the original fabrics are preserved just in few relics of ghost structures. Dolomite crystals typically exhibit concentric to oscillatory zoned luminescence of dark to bright orange, dark to light brown and bright yellow zones (Fig. 12A-D). Some show similar luminescence but of dull to bright red and reddish orange (Fig. 12E). Unzoned, mottled, or blotchy luminescence are almost absent across the succession.

4.3. Dolomite geochemistry

Dolomites have $\delta^{18}O_{dol}$ values from −1.6 to +0.7 and $\delta^{13}C_{dol}$ values from +2.1 to +2.8. While host-rock Limestones have $\delta^{18}O_{lmst}$ values from −3.44 to −0.53 (average: 2.01) and $\delta^{13}C_{lmst}$ values from −0.42 to +5.34 (average: +2.67). Dolostones at Site 866 exhibit $^{87}Sr/^{86}Sr$ ratios between 0.7072880 and 0.7073970 (Fig. 13). The corresponding representative limestone at the same depth range shows $^{87}Sr/^{86}Sr$ ratios between 0.7074490 and 0.7075330. Dolostones have Sr content ranging from 106 to 239 ppm (average: 148 ppm), while limestones Sr content range from 56 to 368 ppm (average: 179 ppm). Dolomite Fe and Mn contents (Fig. 13A-B) range from 70 to 3172 ppm (average: 860 ppm) and 2–49 ppm (average: 17 ppm), respectively. Limestone exhibits Fe and Mn contents (Fig. 13A-B) from 9 to 388 ppm (average: 105 ppm) and 1–28 ppm (average: 11 ppm), respectively. The MgO% plot at Site 866 indicates a lack of partially to fully dolomitised limestone above 1100–1000 mbsf, with a noticeable SiO_2% peak (~68%) at approximately 1075 mbsf (Fig. 14).

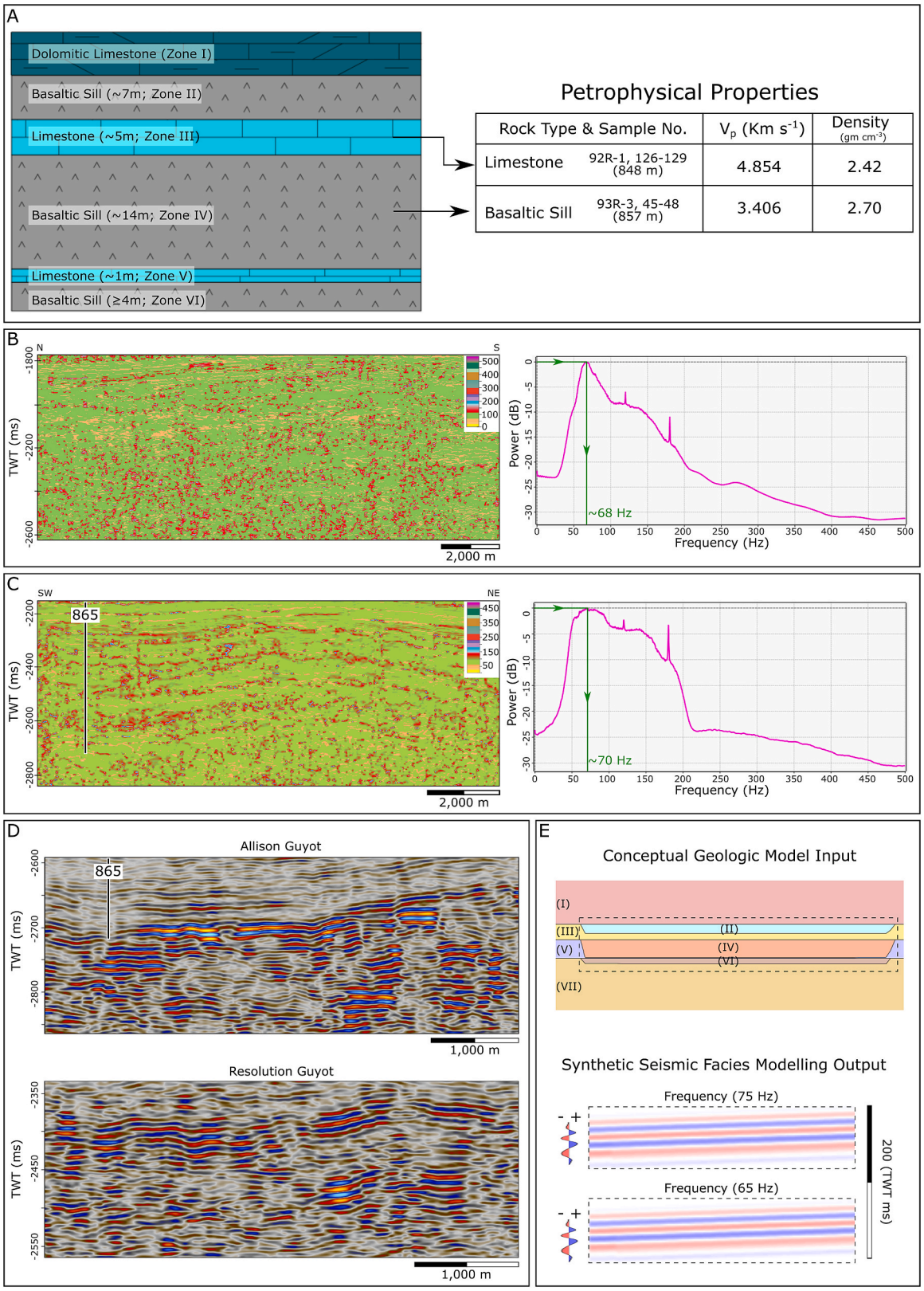


Fig. 6. Seismic facies forward modelling of the interpreted magmatic sill-intrusion. A. A schematic representation of the intruding sill across the sedimentary succession at Site 865 along with their corresponding petrophysical properties. B. and C. Dominant frequency attribute seismic profiles along with spectral analysis data from Resolution and Allison guyots, respectively. A comparison between seismic profiles (D.) displaying the interpreted sills at Resolution and Allison guyots against the results of the seismic facies forward modelling of the conceptual geologic model from core descriptions (E.) at Site 865 using 65 and 75 Hz frequencies, both D. and E. have the same vertical scale. The dashed box in E. highlights the area displayed in the synthetic seismic facies forward models.

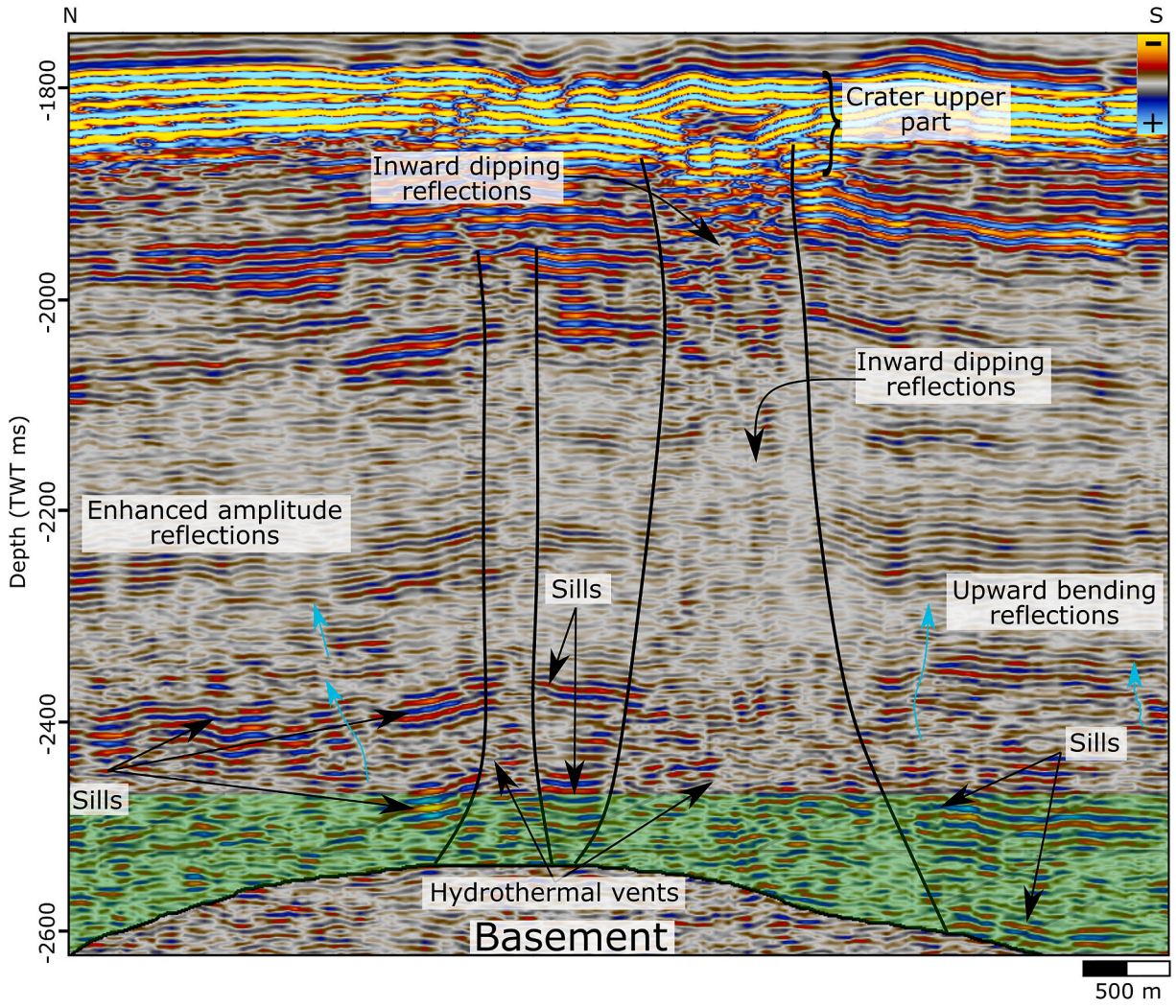


Fig. 7. Seismic interpretation of the magmatic and hydrothermal system in Resolution Guyot. The seismic profile shows the seismic features of SF1: magmatic sill-intrusions (i.e. high amplitude, concordant to locally crosscut relationships within the host-rock strata, sheet-like shape, and abrupt terminations) and their associated SF2: hydrothermal vents and smaller scale fluid flow pipes (i.e. eye-, crater-, mounded-, or dome-shaped geometry of their upper parts, upward bending of surrounding seismic reflections, disrupted reflections within SF2, and their intimate association with underlying magmatic sill-intrusion). The highlighted part with transparent green box represents the approximate depths of the dolomite body(ies) projected away from Site 866.

Interpretation

To explore the age ranges of dolomitisation processes that occurred at Site 866, dolomite $^{87}Sr/^{86}Sr$ isotope ratios were utilised. This involved applying the validation approach outlined by Budd (1997) and Wang et al. (2019), which includes verifying whether these ratios accurately represent the seawater primarily involved in dolomitisation and confirming that no subsequent alterations in the Sr composition occurred within the system. Dolomite Sr content (106–239 ppm; mean 148 ppm) falls below 300 ppm, suggesting an open seawater-buffered diagenetic system. The dolomite $^{87}Sr/^{86}Sr$ ratios generally increase from bottom to top of the dolostone succession, resembling patterns seen in seawater-mediated Cenozoic island dolostones. Their $^{87}Sr/^{86}Sr$ ratios overlap with Mid-Cretaceous Sr-isotope stratigraphy (McArthur et al., 2012). Based on the $^{87}Sr/^{86}Sr$ ages, derived from McArthur et al.'s LOWESS LOOK-UP TABLE 5B, dolomitisation of Early-Cretaceous limestone (depositional age ~132-130 Ma) occurred during the Mid-Cretaceous (125 ± 0.5 to 119.3 ± 1 Ma and/or 112.9 ± 0.35 to 109.5 ± 1.1 Ma; Fig. 13C), indicating ages of at least 5–12 million years younger than the host-rock and 8–15 million years younger than the initiation of sedimentation at Site 866. The possibility of dolostone recrystallisation following the initial dolomitisation phase could reset $^{87}Sr/^{86}Sr$ values and other geochemical aspects as well ($\delta^{18}O_{dol}$, $\delta^{13}C_{dol}$, major and minor elemental composition) which would invalidate dating (Budd, 1997; Wang et al., 2019). However, the following evidence suggests replacement rather than recrystallisation: (a) preservation of depositional fabric and allochem ghosts (Fig. 11), (b) absence of dolomites with markedly different geochemical signatures ($\delta^{18}O_{dol}$, Sr content), and (c) retention of crystal zonation under CL (e.g. Gregg and Sibley, 1984; Lee and Friedman, 1987; Mazzullo, 1992; Machel, 2000a, Fig. 12). Based on integrating dolomitisation age of the shallowest (1224 mbsf) and deepest (1572 mbsf) samples with dolomite $^{87}Sr/^{86}Sr$ values with their depositional age (El-Yamani et al., 2022), the overburden thickness during dolomitisation (125 ± 0.5 to 119.3 ± 1 Ma and/or 112.9 ± 0.35 to 109.5 ± 1.1 Ma) ranged from 425 to 920 and 771–1262 mbsl (metre below sea-level), respectively. Burial and thermal history calculations of the host rock at depths 1224 and 1572 mbsf from initial deposition to 110 Ma are provided in Supplemental Material S3, showing the overburden thicknesses.

By applying Horita's (2014) equation, the lightest and heaviest $\delta^{18}O_{dol}$ of dolomites at Site 866 indicate that the calculated dolomitisation temperatures are rising from 30.4 °C (1224 mbsf: shallowest sample) to 41.2 °C (1572 mbsf: deepest sample). This gradual temperature increase with depth (Fig. 13D) contrasts with typical seawater-mediated island dolostones (e.g. Budd, 1997; Suzuki et al.,

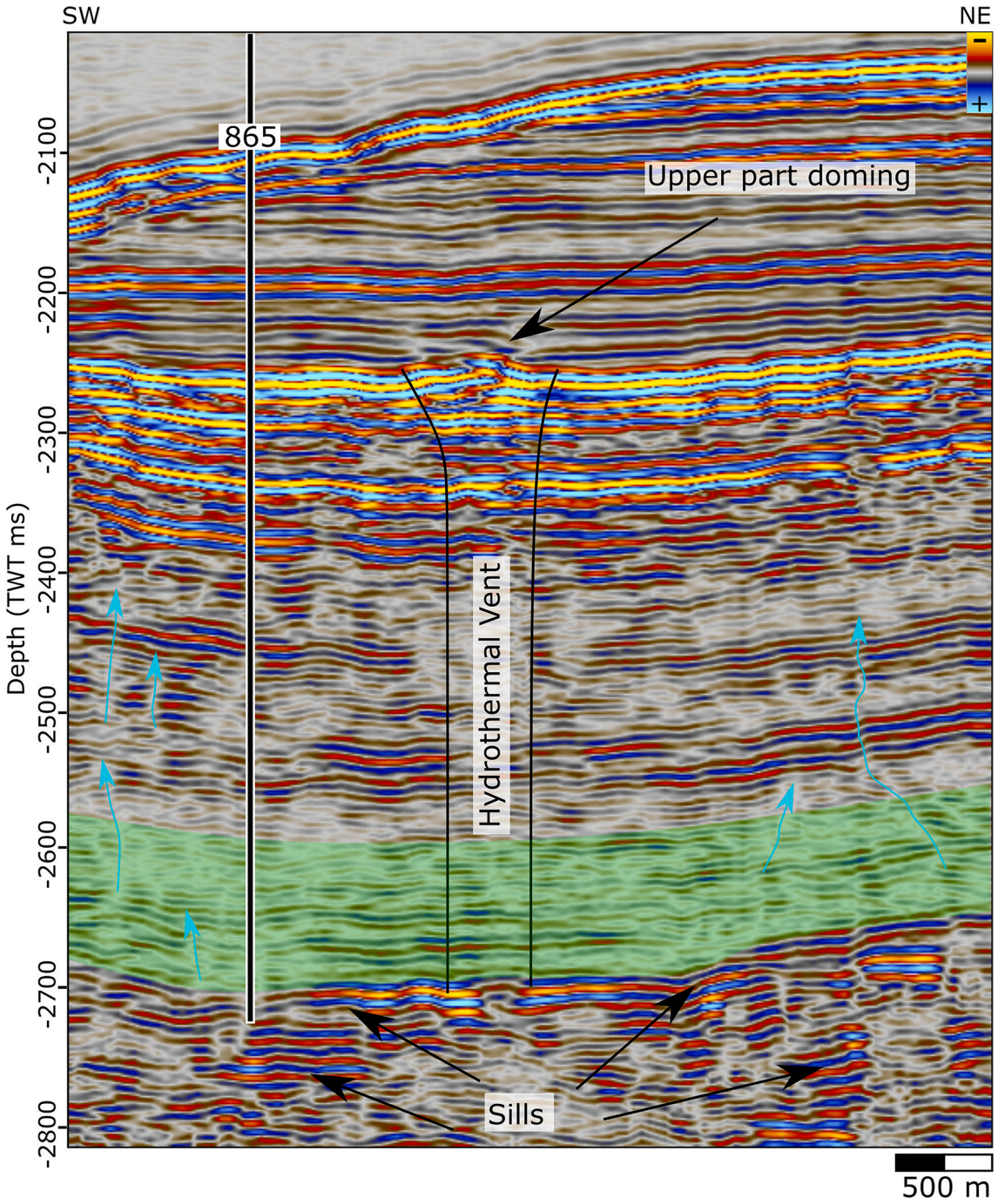


Fig. 8. Seismic interpretation of the magmatic and hydrothermal system in Resolution Guyot. The seismic profile shows the seismic features of SF1: magmatic sill-intrusions (i.e. high amplitude, concordant to locally crosscut relationships within the host-rock strata, sheet-like shape, and abrupt terminations) and their associated SF2: hydrothermal vents and smaller scale fluid flow pipes (i.e. eye-, crater-, mounded-, or dome-shaped geometry of their upper parts, upward bending of surrounding seismic reflections, disrupted reflections within SF2, and their intimate association with underlying magmatic sill-intrusion). The highlighted part with transparent green box represents the approximate depths of the dolomite body(ies) projected away from Site 865.

2006; Ren and Jones, 2016; Wang et al., 2019; Li et al., 2023a). Burial and thermal modelling of the limestone host rock suggests that the concurrent pore-fluid ambient temperatures during dolomitisation (125 ± 0.5 to 119.3 ± 1 Ma and/or 112.9 ± 0.35 to 109.5 ± 1.1 Ma; Fig. 13D; Supplementary Material S1) should have been approximately 14.5–11 °C (Fig. 13D). Elemental data from Resolution Guyot depict host limestone and low Mn, Fe dolomites (Fig. 13A) aligning within the range of seawater island dolomites (Budd, 1997), but with some Fe-rich dolomites concentrated only near the basement (1620–1398 mbsf; ~50% of dolomites with 1536–3172 ppm Fe; mean 2204 ppm; Fig. 13B).

The termination of the dolomitised section aligns with an abrupt peak in SiO_2% (~68%; Fig. 14). This peak could indicate terrigenous input and/or volcanic ashes, given the geological context. However, the lack of correlation between the SiO_2% peak and TiO_2%, Al_2O_3%, or Fe_2O_3% at that level dismisses clastic input (Röhl and Strasser, 1995; Śliwiński et al., 2012). Evidence suggesting that the interval above the pervasive dolomite (1100–1010 mbsf) includes dispersed volcanic ash-rich intervals is: (a) frequency analysis of wireline-logs matches characteristics of volcanic ashes (Watson et al., 2017) with 77% of RHOB log falling between 2.15 and 2.35 gm/cm^3, 58% of NPHI log

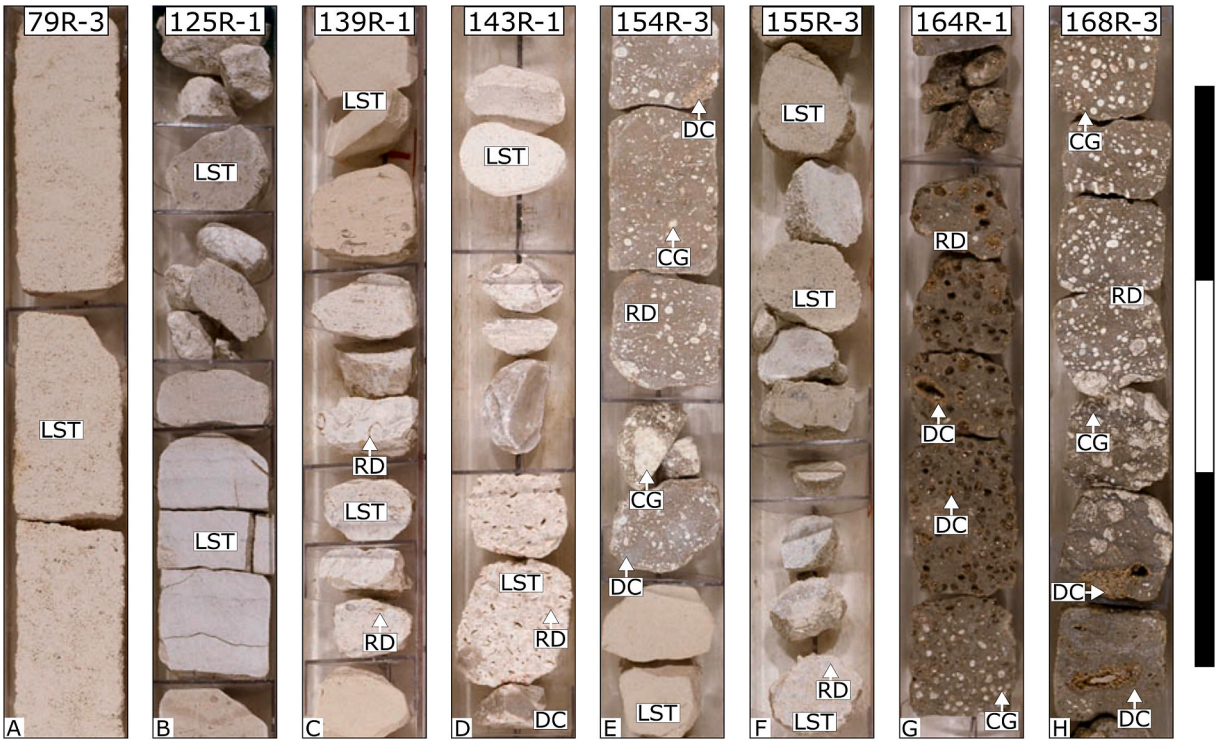


Fig. 9. Core photographs of the dolomitised succession at Site 866, Resolution Guyot. The scale bar represents 30 cm. The naming of the cores is as follows: core number, core type (R: rotary coring), & section number. A. Core photo showing the beige and cream hues of limestone (LST) oolitic grainstone (738 mbsf). B. Core photo showing light brown partially dolomitised limestone (LST) of peloidal bioclastic grainstone (1174 mbsf). C. Core photo of beige colour of patchy dolomitised limestone of peloidal wacke-to pack-stone with few replacive dolomites (RD) (1309 mbsf). D. Core photo showing in the upper part non-dolomitised limestone (peloidal and oolitic grainstone) while the lower part is dolomitised with replacive dolomites and dolomite cement (1358 mbsf). E. Core photo of dark brown dolostone with preserved calcitic grains, dolomite cements, and replacive dolomites. The lower part of the photo shows non-dolomitised limestone (1457 mbsf). F. Core photo of light brown colour of peloidal grainstone of partially dolomitised limestone (1468 mbsf). D, E, & F represent partially-totally dolomitised intervals alternating with limestones. G. Massive dolostone of oncoidal and oolitic pack- and grain-stone (1550 mbsf). The photo shows calcitic grains, replaced grains with dolomites, and mouldic porosities of dissolved ooids and onocolites which are filled totally or partially with dolomite cements. H. Core photo of massive dolostone of oncoidal and oolitic grain- to rud-stone. (1592 mbsf). The photo shows calcitic grains, replaced grains with dolomites, and mouldic porosities of dissolved ooids and onocolites which are partially or totally filled with dolomite cements.

between 30 and 39 pu, and 62% of DTLN between 80 and 100 us/ft; (b) silica content at ~1080 mbsf (~69%) fits within the suggested range for volcanic ashes (45–75 wt%; Heiken, 1972); (c) fragments of volcanic glass are observed at 1010–1040 mbsf (Röhl and Strasser, 1995); (d) low Cr concentration (≤1 ppm) matches values of discrete ash layers (<3 ppm; Sigurdsson et al., 1997); (e) the presence of varicolored (green–grey) smectitic, illitic, and I/S mixed-layer clays (Baudin et al., 1995); (f) their host-rock limestone has mid-late Barremian age which overlap with the proposed volcanic ash origin of the Barremian and Aptian clays at Site 463 (25 km east of Resolution Guyot; the Barremian-Aptian volcanism in the western Pacific; Vallier and Jefferson, 1981).

5. Discussion

5.1. The link between magmatism and hydrothermal venting

Previous studies on different types of hydrothermal vents complexes across different types of sedimentary basins interpreted their origin as 'volcanic features' (Skogseid et al., 1992; Davies et al., 2002). However, subsequent studies, based on integrating wireline-logging data and 3D seismic data, suggested that hydrothermal vents above sills are formed predominantly through hydrothermal fluid circulation and subsurface remobilisation of sediments rather than extrusive seafloor volcanism (Bell and Butcher, 2002; Planke et al., 2005). The origin of hydrothermal vent complexes (SF2) in this study is deduced through seismic facies analyses, exhibiting distinct characteristics compared to the host-rock (Figs. 5, 7, and 8): (a) cylindrical low amplitude conduits, (b) eye-, crater-, mounded- or dome-shaped upper parts, (c) internal inward-dipping reflections, (d) preferred locations of hydrothermal vents at the tips of magmatic sills. These seismic features resemble hydrothermal vent complexes in other settings linked with magmatic intrusions that mobilise fluids, leading to fracturing of overlying strata (e.g. Jamtveit et al., 2004; Planke et al., 2005; Hansen, 2006). To form these complexes, local fluid pressure must exceed hydrostatic pressure, generated through the following factors (Judd and Hovland, 2007; Planke et al., 2005; Aarnes et al., 2012; Iyer et al., 2017; Omosanya et al., 2018; Wang et al., 2018c): (a) temperature increase by the magmatic sill-intrusions would rapidly heat the surrounding rocks causing boiling of pore-fluids, (b) magmatic release of H_2O–CO_2–SO_2–HCl-rich hydrothermal fluids from the intruded magma would cause overpressure, (c) metamorphic dehydration reactions between magmatic intrusions and host-rock would release various gases (e.g. CO_2 and SO_2), (d) generation of large quantities of other gaseous such as CH_4 could result in large overpressures. As pressure cannot be dissipated quickly, areas around the magmatic sill-intrusions would become overpressured and hydraulic fracture networks would form hydrothermal vent complexes and associated smaller scale fluid escape pipes along which gas, water, magmatic fluids, and volatiles would escape to the seafloor (Roelofse et al., 2021). The previously described factors were seen at Resolution and Allison guyots. At Site 865, the contact between sills and overlying carbonates reveals decarbonated, metasomatised, lignite-bearing sedimentary layers that contains fragments of very highly to completely altered basalts due to high intrusion temperatures (Sager et al., 1993b). Site 866 displays a negative $\delta^{34}S_{CAS}$ shift (125-110

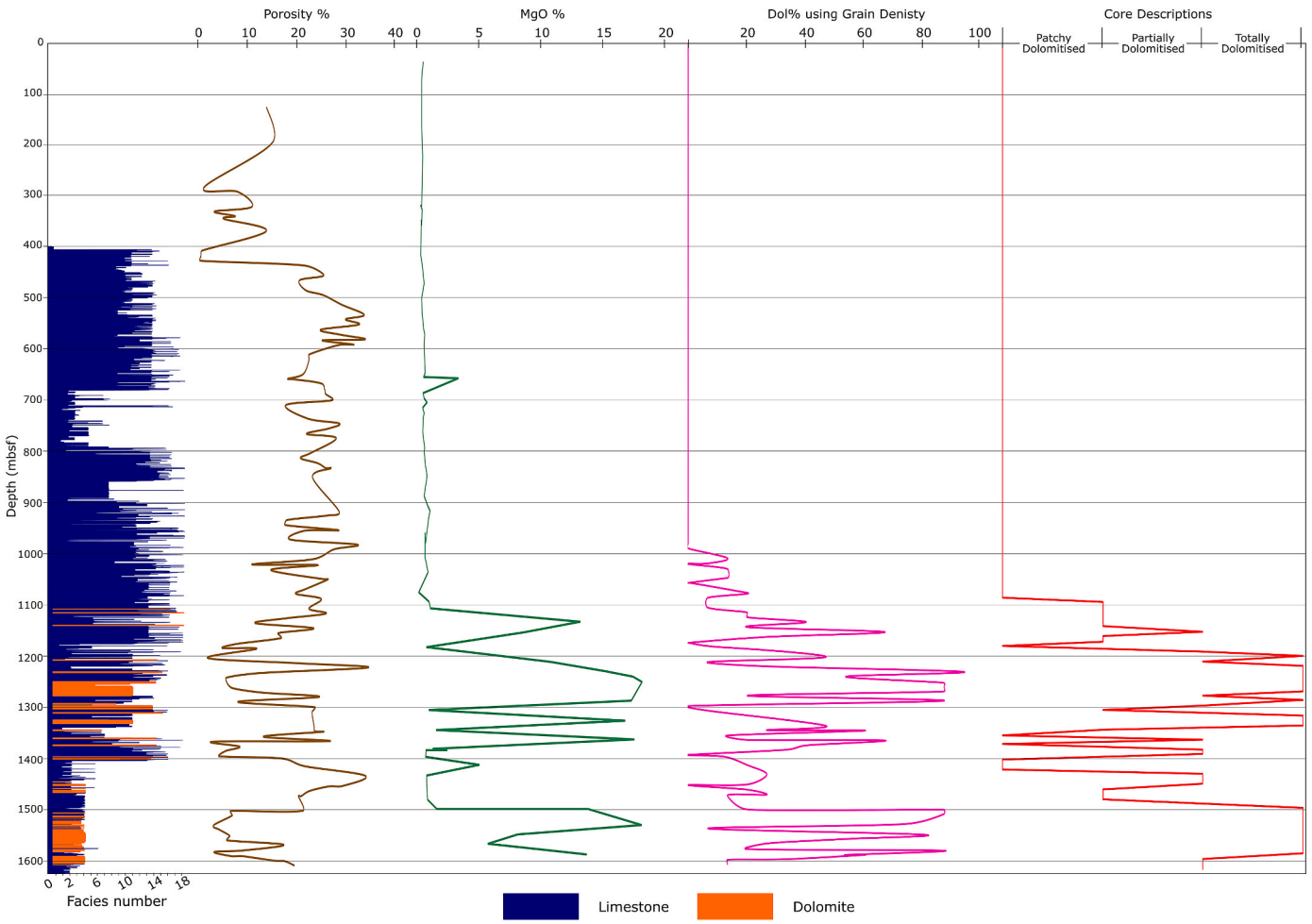


Fig. 10. Dolomite distribution versus depth at Site 866 based on integrating core descriptions, MgO%, and dolomite% using grain density along with measured porosities (Sager et al., 1993a) and facies templates (Arnaud et al., 1995). The green boxes highlight the dolomitised intervals. Facies numbers, based on (Arnaud et al., 1995), are: Facies 0: Fine-grained Pelsparites, Facies 1: Peloosparites and Oopelsparites with Reworked Ooids, Facies 2: Well-sorted Oosparites to Oomicrites, Facies 3: Peloosparites and Peloomicrites, Facies 4: Oo-oncosparites with Rounded Micritic Oncoids, Facies 5: Pelsparite and Pelmicrite with Echinoderm Plates and Small Benthic Foraminifers, Facies 6: Coarse-grained Biosparites with Rounded Elements, Facies 7: Coarse-grained Biosparites with Rudist and Gastropod Shells, Facies 8: Pelbiomicrites and Pelbiosparites with Benthic Foraminifers, Facies 9: Micrites and Pelmicrites with Sponge Spicules and Large Benthic Foraminifers, Facies 10: Micrites and Biomicrites with Large Foraminifers, Facies 11: Micrite and Pelmicrite with Rudists and Gastropods, Facies 12: Micrite and Pelmicrite with Green Algae, Facies 13: Micrite with Ostracodes and Small Benthic Foraminifers, Facies 14: Micrite and Pelmicrite with Bird's Eyes, Facies 15: Micrite and Pelmicrite with Oncolites, Facies 16: Micrite-Pelmicrite and Dolomicrite-Dolopelmicrite with Algal-Microbial Mats, Facies 17: Micrite and Dolomicrite with Thin Sedimentary Laminations, Facies 18: Micrite with Desiccation Cracks.

Ma), suggesting increased volcanism, hydrothermal activities, and magmatic sulphur release (Mills et al., 2017; Paytan et al., 2004). Relatively high T_{max} values at Site 865 and charcoal content at Site 866 (Baudin et al., 1995) imply thermal anomalies caused by basaltic sills. In addition, our interpretation of the seismic data revealed the absence of any volcanic cones or lava flows (e.g. Infante-Paez and Marfurt, 2018) related to the interpreted hydrothermal vents at both guyots. Hence, hydrothermal vent complexes above the sills in both guyots resulted from hydrothermal fluid circulation and hydraulic fracturing of sediments rather than extrusive seafloor volcanism.

5.2. *Magmatically driven hydrothermal dolomitisation*

Fe and Mn concentrations can provide one of the most useful types of information regarding interpretations of dolomite genesis (James and Jones, 2015). Modern seawater typically contains low Mn (0.2 ppb) and Fe (2 ppb; Drever, 1997). According to Veizer (1983), dolomites formed in seawater should exhibit low Mn (1 ppm) and Fe (3–50 ppm). Seawater-mediated island dolomites are known for low Fe (<300 ppm) and Mn (<50 ppm) concentrations (Budd, 1997). However, the lowermost 220 m of Cretaceous dolomitic limestones and dolostones at Resolution Guyot exhibit notably high Fe content (range: 1536–3172 ppm; mean: 2204 ppm), suggesting external metal sources like overlying soil, underlying volcanics, or detrital siliciclastics (Budd, 1997). Soil horizons, exposure surfaces are not likely the source here as the observed Fe-enrichment cannot be explained by Fe-stained exposure surfaces (e.g. Fe of few hundreds of ppm in dolomites around soil horizons and exposure surfaces in Grand Bahama Island and the Xisha islands; Budd, 1997; Li et al., 2023a). The correlation between terrigenous input proxies (SiO_2%, TiO_2%, Al_2O_3%, Fe_2O_3%; Fig. 14) around ~1400-1380 mbsf suggests terrigenous input, supported by dispersed clay seams in cores. Therefore, this might suggest terrigenous input as the source of Fe-enrichment at that level. However, this cannot explain the Fe-enrichment below 1400 mbsf (Fig. 14) because (a) there is no correlation between terrigenous input proxies below that level except at ~1552 mbsf which correspond to a very small, millimetres-thick, clay seam, (b) clay seams are very rare in the cores with millimetre-centimetre scale, and (c) XRD analyses at Site 866 suggest absence of any clayey interbeds between 1400 and 1601 mbsf (Murdmaa et al., 1995). Thus, this rules out terrigenous input as a source of

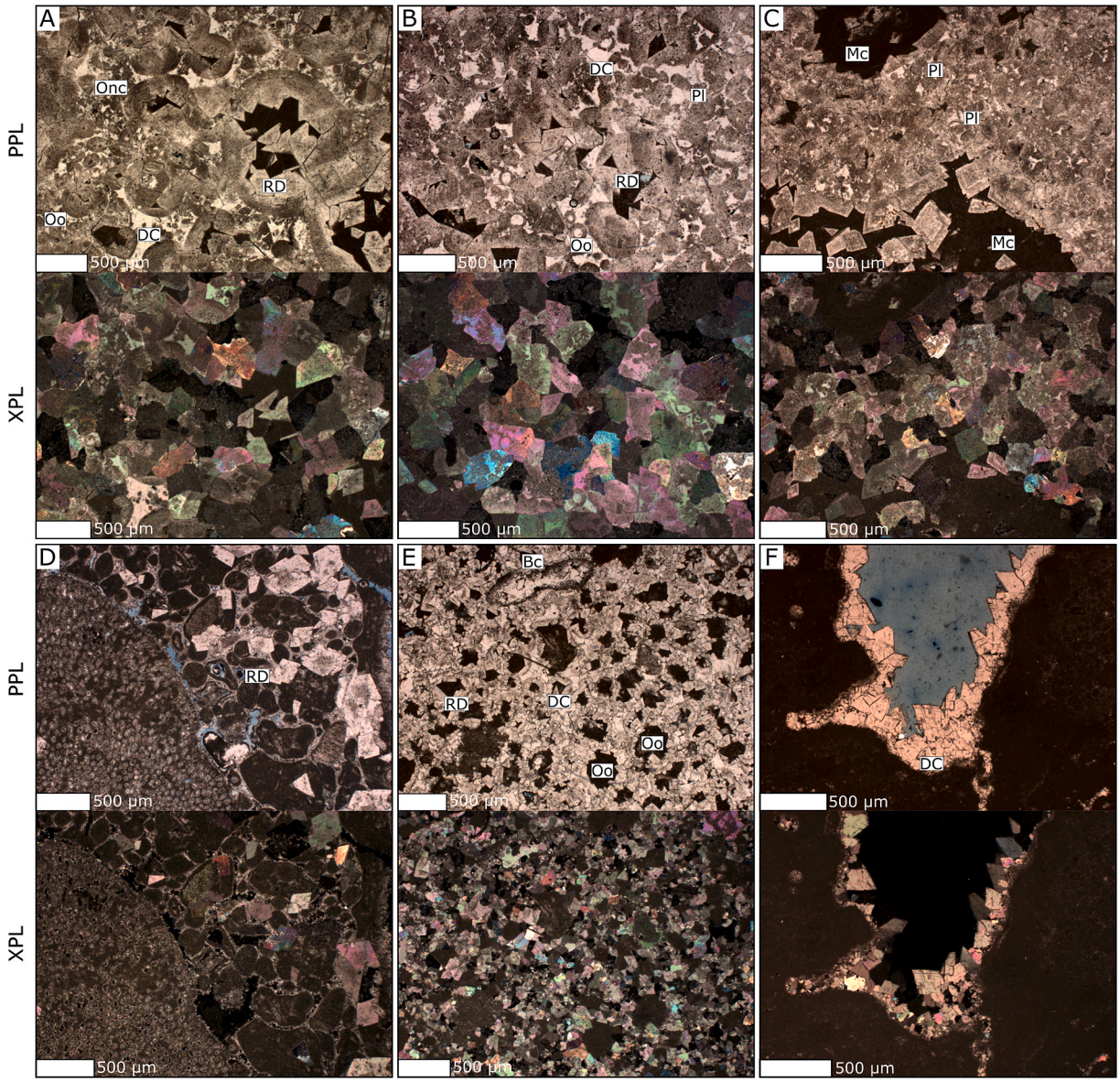


Fig. 11. Thin-section photomicrographs showing plane polarised light (PPL) and crossed polarised light (XPL). A. & B. Photomicrographs from totally dolomitised intervals showing replacive dolomites (RD) and dolomite cement (DC) with fabric preservation of ooids (Oo), oncoids (Oc) and peloids (Pl). C. Photomicrograph from partially dolomitised interval showing outlines of original fabric and partially dolomitisation of muddy matrix (Mc). D. Patchy dolomitised limestone. E. Pervasively dolomitised limestone with fabric preservation. F. Partially filled vug with dolomite cement in a wackestone.

Fe-enrichment below 1400 mbsf. Therefore, the volcanic basement is the only plausible source left for Fe-enrichment at ~1620-1540 mbsf. The depths of dolomites (Figs. 4 and 7C, D) at Allison (−2707 to −2596 TWT ms; 660–837 mbsf) and Resolution (−2790 to −2490 TWT ms; 1620–1050 mbsf) guyots and the depths of the interpreted sills on seismic data are laterally overlapping which suggests spatial coexistence. Moreover, there is a strong temporal overlap between (a) the $^{87}Sr/^{86}Sr$ ages of dolomites, (b) the ages of basalt samples at Site 866 (107–125 Ma using K/Ar whole-rocks age dating and an average of 126 Ma using $^{40}Ar/^{39}Ar$ age dating, Baker et al., 1995; Pringle and Duncan, 1995; Sager, 1995), (c) the negative $\delta^{34}S_{CAS}$ shift at Site 866 (110–125 Ma; Mills et al., 2017), and (d) the proven magmatism at the Mid-Pacific Mountains (130-110 Ma; Pockalny et al., 2021) which may suggest a causality relationship (Fig. 13C). Based on the dolomitisation age of the shallowest (1224 mbsf) and deepest (1572 mbsf) samples with dolomite $^{87}Sr/^{86}Sr$ values, the range of the overburden thickness during dolomitisation was 425–920 and 771–1262 m, respectively. Such an overburden thickness suggests post-depositional dolomitisation within depths of shallow to intermediate burial diagenetic settings (sensu Machel, 1999). This does not support syndepositional or near-surface early-burial dolomitisation by normal to seasonally evaporative seawater as suggested earlier (Sager et al., 1993b; Röhl and Strasser, 1995; Strasser et al., 1995). The $\delta^{18}O_{dol}$ calculated temperatures are ~18–29 °C hotter than the concurrent temperatures of the host rock (Fig. 13D) given that the proven active exchange between pore-water and surrounding seawater at the Pacific guyots (Paull et al., 1995) should have driven the temperatures within the guyots towards the surrounding seawater temperatures (i.e. negative geothermal gradient in oceanic islands and atolls mimicking those of the open marine profile as observed in Enewetak, Bikini, Kita-daito-jima, Fangataufa, and Mururoa atolls, Reed Bank, Tahiti, and Grand Cayman Islands, Florida Platform, and Yucatán Peninsula; Swartz, 1958 ; Kohout et al., 1977; Rougerie and Wauthy, 1993; Guille, 1996; Henry et al., 1996; Andrié et al., 1998; Fairhurst et al., 1999; Leclerc et al., 1999; Jean-Baptiste and Leclerc, 2000; Jones et al., 2000; Warren, 2000; Stoessell et al., 2002; Steinmann and Déjardin, 2004; Montaggioni and Braithwaite, 2009; Ren

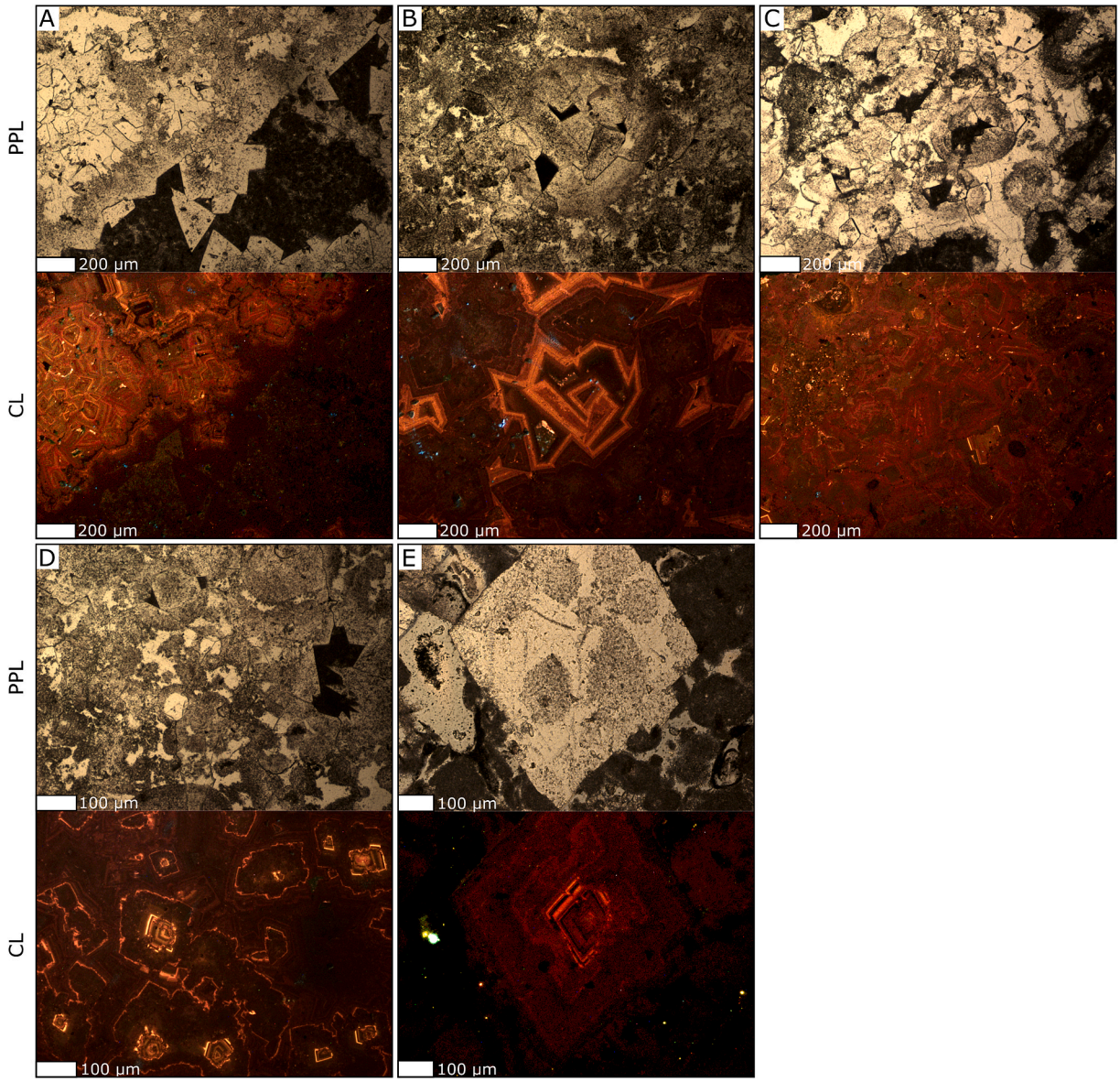


Fig. 12. Thin-section photomicrographs showing plane polarised light (PPL) and cathodoluminescence (CL). Concentric to oscillatory zoned luminescence of dark to bright orange, dark to light brown (A–D) and bright yellow zones (D). E. Concentric to oscillatory zoned luminescence of dull to bright red and reddish orange.

and Jones, 2017; Wang et al., 2020). Using other published equations of oxygen isotope fractionation during dolomitisation to compute $\delta^{18}O_{dol}$ temperatures (Northrop and Clayton, 1966; O'Neil and Epstein, 1966; Fritz and Smith, 1970; Sheppard and Schwarcz, 1970; Matthews and Katz, 1977; Land, 1985; Woronick and Land, 1985; Vasconcelos et al., 2005; Müller et al., 2019; Supplementary Sheet T12) would change the absolute values of $\delta^{18}O_{dol}$ derived temperatures but it does not change the conclusion that dolomitisation temperatures are hotter than concurrent temperatures of the host-rock with at least 12–25 °C. Our calculations are conservative considering that if the $\delta^{18}O_{water}$ was changed by the interaction of normal Cretaceous seawater (0.2‰ SMOW; Zhou et al., 2008) with magmatic fluids (5.3–10‰ SMOW; Sahlström et al., 2019), then the temperature of dolomitisation could be significantly higher than estimated. Therefore, this suggests the presence of an external heat source (sensu hydrothermal dolomite; Machel and Lonnee, 2002).

Accordingly, our integration of geochemical, seismic, and wireline-logging data at Resolution Guyot led us to propose a magmatically driven hydrothermal dolomitisation model (Fig. 15) which is suggested to be applicable as well in Allison Guyot based on the similar geologic setting and the association between sills and dolomites (Figs. 7 and 8). Three main contributions of magmatic emplacement to facilitate dolomitisation have been inferred from our study. Firstly, magmatic activities, including sill emplacement, and the resultant magmatic-hydrothermal fluids, have contributed significantly to boosting thermal energy, driving increased seawater circulation through the atolls, thereby acting as a high heat flux source. In general, the average basal heat flux of magmatically passive oceanic island crusts have a range of ~60–101 mW/m^2 (Henry et al., 1996; Leclerc et al., 1999; Jean-Baptiste and Leclerc, 2000; Turcotte and Schubert, 2001; Wilson et al., 2001). To estimate the basal heat flow at Resolution Guyot, we used the compiled dataset by Stein and Stein (1992) which relate the heat flow to the age of the oceanic crust. Considering the deposition began at Site 866 at ~132–133 Ma (El-Yamani et al., 2022), indicating the volcanic pedestal's age beneath the atoll is at least that old. This corresponds with the magnetostratigraphic zonation observed in the sedimentary layers at Site 866 (Tarduno et al., 1995), where the base of the sedimentary sequence is placed within Chron M7 (around 132-132.55 million years

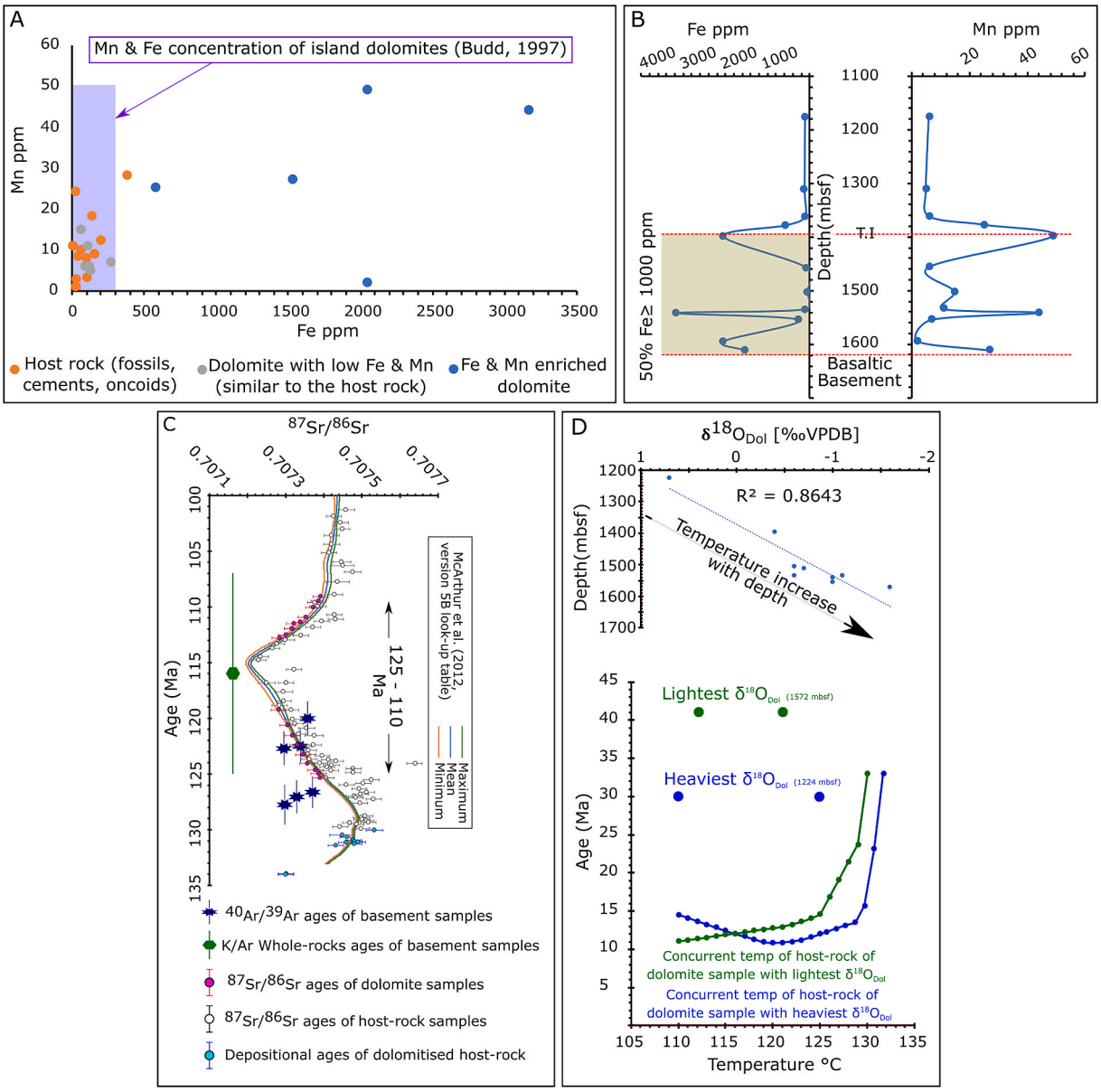


Fig. 13. Geochemical analyses of the dolomite at Site 866. A. Mn and Fe plot showing a cluster of the host rock and low Fe and Mn dolomites within values of island dolomites by Budd (1997) and presence of Fe-enriched dolomites. B. Fe and Mn plot with depth showing Fe-enrichment of the dolomite close to the basement. The dashed line in panel (B) shows the location of the potential terrigenous input (T.I). C. Depositional age model of the host rock (El-Yamani et al., 2022) and the $^{87}Sr/^{86}Sr$ ages of the dolomite and $^{40}Ar/^{39}Ar$ ages of the basement and K/Ar whole-rock ages of the basement (Baker et al., 1995; Pringle and Duncan, 1995). D. $\delta^{18}O_{Dol}$ vs depth showing temperature increase with depth which is different form the expected thermal history of host rock at 1572 and 1224 mbsf between 125 and 110 Ma.

ago, according to the geological time scale 2012 by Ogg, 2012). This suggests that the basement must be of at least that age or older. As the age of basalts at the same site is average ~126 Ma (Pringle and Duncan, 1995; Sager, 1995), the minimum quiescence time before magmatism recommenced and the youngest possible age of the volcanic pedestal during subsequent magmatism would be ~6–7 million years. Consequently, the highest possible basal heat flux from the pedestal, before magmatic rejuvenation at ~126 Ma, would be at most ≤ 100 mW/m^2 (using Stein and Stein, 1992 database; check their Fig. 1), falling within the known ranges of basal heat flux in magmatically passive oceanic island crusts. This is much lower than the heat flux at regions where magma ascends and hydrothermal circulation occurs (e.g. >800–2000 mW/m^2 Leroy et al., 2010; Pearson-Grant et al., 2022). Such surge occurs because the emplacement of magmatic intrusions and basaltic lavas generates temperatures ≥1000–1350 °C (Parfitt and Wilson, 2009; Clague et al., 2018; Shea et al., 2022), significantly influencing the local heat flow dynamics. This explains the higher temperatures of the dolomites at Site 866 compared to the concurrent temperatures of the host rock, and the strong temporal overlap between the dolomitisation $^{87}Sr/^{86}Sr$ ages and $^{40}Ar/^{39}Ar$ and K/Ar ages of basement samples. Numerical modelling by Jean-Baptiste and Leclerc (2000) and Frazer et al. (2023) emphasised the positive impact of the increase in the basal heat flow on the fluid flux velocities across the carbonate platforms. Similarly, reactive transport modelling of early-burial island dolomitisation by geothermal convection showed that the increase of basal heat flux from 40 to 100 mW/m^2 would double the dolomitisation rate (Whitaker and Xiao, 2010). Accordingly, the magmatism in Resolution Guyot had important impacts on the fluid flux and the temperature to overcome the very limited dolomitisation potential and dolomitisation rates of normal Cretaceous seawater (Gabellone and Whitaker, 2016).

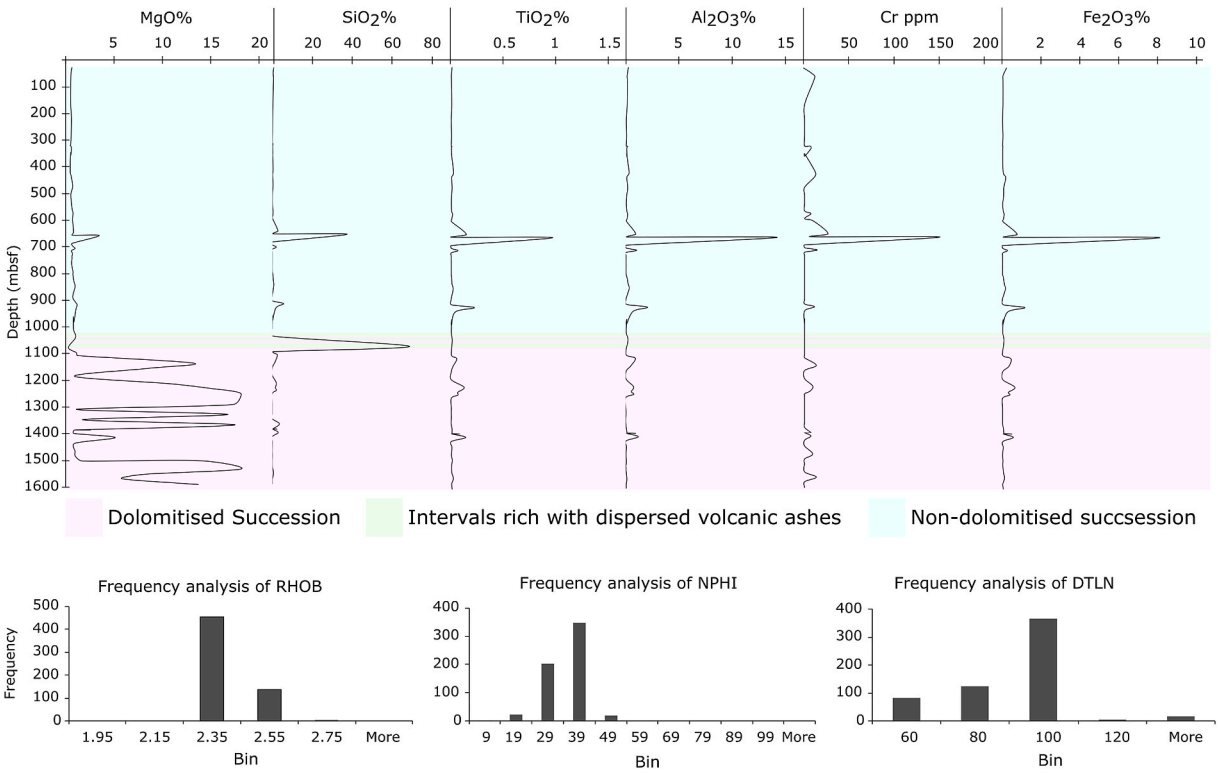


Fig. 14. Geochemical analysis plot at Site 866 showing the presence of dolomites between 1620 and 1100 with absence of dolomite above that level. It also shows the peak of SiO_2% above the dolomites with no correlation with TiO_2%, Al_2O_3%, Fe_2O_3%, and Cr ppm. The figure shows the frequency analysis on log interpretation showing that the interval between 110 and 1010 mbsf is characterised by (1) 77% of RHOB is ~2.15–2.35 gm/cm^3, (2) 58% of NPHI is ~30–39 pu, and (3) 62% of DTLN is ~80–100 us/ft.

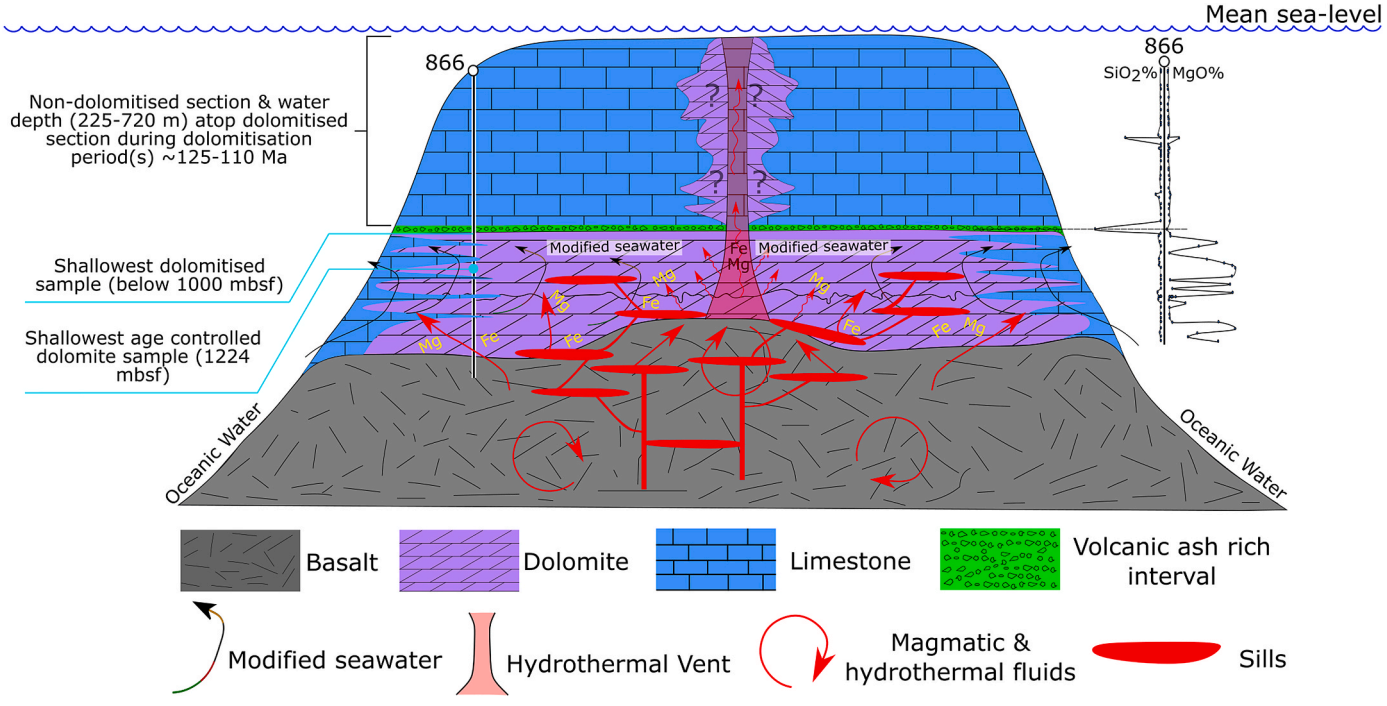


Fig. 15. Conceptual model of the sills emplacement, hydrothermal vents and the released magmatic fluids interacting with the basement leaching Fe and Mg to the circulating seawater causing a slight modification of its metal content, increasing the Mg^{2+} budget, Mg/Ca ratio, and temperature which facilitated dolomitisation. The dispersed intervals rich with volcanic ash acting as an aquiclude to the upflow of the dolomitising fluids. The model shows the expected dolomite distribution away from the drilling site based on the presence of preferentially dolomitised intervals at the drilling site.

Secondly, the ongoing discussion showed that the seismically interpreted hydrothermal vents, and smaller scale fluid flow pipes in both atolls were magmatically originated through hydraulic fracturing. They have width ranges of few to tens of hundreds of metres (Figs. 3, 7 and 8). However, previous modelling and field-based studies suggested that individual active hydrothermal vents widths are significantly narrower (5–10 m) than what is observed in seismic data (Collignon et al., 2018; Manton et al., 2022). Therefore, what appears on seismic data to be relatively wide conduits with width of hundreds of metres was suggested to represent amalgamated vent structure of highly fractured rock masses (Huuse et al., 2010; Manton et al., 2022). This would suggest that the widespread presence of hydrothermal vents and smaller scale fluid pipes in both atolls would reflect the presence of highly fractured rock masses across the atolls. This fracturing would enhance the fluid flux across the atolls and so the dolomitisation reactivity as observed in (a) the reactive transport modelling results showing that the presence of a permeable platform margin fault zone enhances dolomitisation on the upper slope and margin, and to a lesser but significant extent, across platform interior (Frazer et al., 2023) and (b) field-studies (e.g. Hammam Faraun stratabound dolostone bodies, Gulf of Suez; Hirani et al., 2018).

Thirdly, our study suggests that the underlying volcanic basement is likely the source for Fe-enriched dolostones at ~1620-1540 mbsf. Fe solubility in seawater from basaltic rocks depends on pH, oxygen, redox potential, temperature, and organic ligands (Hemley et al., 1992; Heinrich and Candela, 2014). Mg and Fe are contained in pyroxene and olivine minerals whose dissolution rates decrease with increasing pH (Gudbrandsson et al., 2011). Neutral pH keeps Fe as insoluble oxyhydroxides (Stranghoener et al., 2018). Therefore, injection of acidic CO_2-charged fluids into crystalline basalts would favour metals mobility (e.g. Mg and Fe; Caruso et al., 2021). During magmatism, highly acidic magmatic H_2O–CO_2–SO_2–HCl-rich fluids discharge and mix with seawater during upflow (Seewald et al., 2015; Wilckens et al., 2019). Even mixing a small volume of magmatic-hydrothermal fluids with predominantly normal seawater would lower the fluid's pH (Breislin et al., 2020). This promotes mafic mineral alteration in basalts, leaching metals like Mg and Fe (Gamo et al., 1997; Gudbrandsson et al., 2011; Caruso et al., 2021), enriching seawater. Considering that, the temporal overlap between dolomitisation age, basaltic basement ages, and the negative $\delta^{34}S_{CAS}$ shift at Site 866 and the presence of Fe-rich dolomites just close to the basement (~1620-1540 mbsf) may suggest that seawater underwent slight modification by slight mixing with magmatic-hydrothermal fluids, facilitating leaching metals (Fe and Mg) from the basement. This slight modification of seawater by mixing with magmatic-hydrothermal fluids would promote dolomitisation at both atolls because (a) localised seawater acidification was proposed to promote dolomitisation (Rivers et al., 2021; Rivers, 2023) and (b) leaching of Mg from mafic minerals in basalts would locally elevate the Mg^{2+} concentration and Mg:Ca ratio of the dolomitising fluid (Robertson et al., 2019; Breislin et al., 2020; Koeshidayatullah et al., 2020). These, coupled with higher water temperature (e.g. Benjakul et al., 2020 and pCO_2 e.g. Sibley, 1990) would counteract three significant kinetic inhibitors: cold seawater and the low Cretaceous seawater Mg^{2+} concentration and Mg:Ca ratio.

Basalts in Resolution Guyot are highly altered (average MgO wt% of 4.8 and FeO wt% of 1.5; Kurnosov et al., 1995). Appropriate fresh analogues for the West Pacific Guyots are the Hawaiian ocean island basalts (Kurnosov et al., 2007) which have average MgO wt% of 12.3 and FeO wt% of 11.9 (Dasgupta et al., 2010). This alteration of the basaltic rocks of the West Pacific Guyots was attributed to hydrothermal processes and subaerial weathering (Kurnosov et al., 1995, 2007) . In Allison Guyot, although the basaltic basement was not drilled, intensive hydrothermal alteration is observed in magmatic sills with an average MgO wt% of 5.5 and an average FeO wt% of 2.2 ; (Kurnosov et al., 1995, 2007). The porous nature of the basement, characterised by vesicular and fractured lavas (Sager et al., 1993a), supports the potential of circulation of slightly modified seawater.

5.2.1. Controls on dolomitisation distribution

Our integrated approach of delineating the distribution of dolomitised intervals at Resolution Guyot (Fig. 10) appears to reflect that their distribution seems to be controlled on both local and large scales. On large scale, during the dolomitisation period(s) at Resolution Guyot, our burial history calculations reflect that at least ~220–720 m of limestone above the dolomitised succession did not undergo dolomitisation (Supplemental Material S3). This raises a question about why the overlying succession wasn't dolomitised, especially that geothermal convection dolomitisation operates across the entire thickness during the dolomitisation period, as observed in field (e.g. Aharon et al., 1987; Vahrenkamp and Swart, 1994) and reactive transport modelling (e.g. Whitaker and Xiao, 2010; Frazer et al., 2023) studies. Two potential explanations arise for this distribution. The first possibility is that the dolomites at Resolution Guyot might exhibit mushroom-shaped structures as in (a) the Latemar Platform (Wilson et al., 1990) and (b) the modelling results of dolomitisation by geothermal circulation of brines (Pal et al., 2015) or it might be controlled by igneous intrusions, their associated brecciated contacts, and fractures (Jacquemyn et al., 2014). However, the absence of additional drilling sites across the platform prevents the verification of this hypothesis. The second possibility is that there could be an aquitard which might have impeded fluid flow above this level and focused the fluid flow within the dolomitised part. This hypothesis appears more plausible considering the correlation we observe between the termination of dolomitisation (~1100-1010 mbsf) and the identified dispersed volcanic ash-rich intervals (Fig. 14). Volcanic ashes and their altered clays can occlude pore spaces, creating a baffle, as seen in the diagenetic fronts in the Tengiz Field (Kenter et al., 2006; Dickson and Kenter, 2014).

At a local scale, dolomitisation is seen within a ~570-600 m section of dolomitic limestone and dolostone, occurring at specific levels rather than uniformly throughout (Figs. 3 and 10; Supplemental Sheet T8). In general, preferential dolomitisation is often controlled by permeability pathways: (a) certain intervals with higher permeability that focus fluid movement (e.g. karstified or fractured intervals; Li et al., 2023a; Hirani et al., 2018), or (b) variations in the mineralogy and texture of sediment types (e.g. Saller et al., 2001; Whitaker and Xiao, 2010). Our examination of dolomite distribution with the sedimentary facies template at Site 866 (Arnaud et al., 1995) shows no correlation which suggests that textural or facies controls are less likely. Dolomites are found across various lithofacies, from wacke- and pack-stone to grain- and rud-stone (Fig. 10), and the same in the non-dolomitised sections. Additionally, measurements of porosity reveal no link between tight zones and non-dolomitised sequences. The non-dolomitised sections between dolomitised intervals at Resolution Guyot exhibit a wide range of interparticle porosities (4.5–27.25%; mean: 18.7%; Kenter and Ivanov, 1995). Permeability can be derived from Interparticle porosity in non-vuggy carbonate rocks based on Lucia's (1995) equations. By using the three different equations of Lucia's (1995) for the different rock classes, the non-dolomitised grainstone-dominated intervals have estimated permeability of $1.2 - 68 \times 10^3\ md$ (median: $7.2 \times 10^3\ md$; average: $16.5 \times 10^3\ md$), non-dolomitised packstone-dominated intervals have estimated permeability of $5 \times 10^{-3} - 3.9 \times 10^2\ md$ (median: $1.7 \times 10^2\ md$; average: $1.8 \times 10^2\ md$), and wacke- and mud-stone dominated intervals have estimated permeability of $\leq 1\ md$ (Supplemental Sheet T14). Results from reactive transport modelling by Whitaker and Xiao (2010) on early-burial geothermal convection dolomitisation indicate that permeabilities ranging from tens to tens of thousands of millidarcies are sufficient for convective fluid flow and suitable for geothermal convection dolomitisation. Accordingly, the non-dolomitised pack- and grain-stone-dominated intervals at Resolution Guyot possess permeability ranges suitable for this process, as opposed to the wacke- and mud-stone dominated intervals. However, despite adequate permeability, these intervals remain non-dolomitised. Therefore, the control through fractures becomes the most probable scenario. Our earlier

discussions suggested the formation of hydrothermal vents through hydraulic fracturing. Consequently, the distribution and density of fracture networks around and away from vents may have governed fluid movement, creating pathways for fluid flow and leading to the observed dolomitised bodies at specific levels in Resolution Guyot.

5.3. Implications on island dolomitisation and normal marine dolomitisation by the Cretaceous calcitic seawater

The findings of this study exhibit both differences and similarities with dolomitisation models for Cenozoic island dolostones. Most studies on Cenozoic island dolostones propose dolomitisation by normal seawater (e.g. Budd, 1997; Warren, 2000; Ren and Jones, 2018). However, Machel, 2000b introduced an alternative concept for Cenozoic island dolomitisation involving plate tectonics-induced convection of seawater that was enriched by magmatic-hydrothermal solutions. Our proposed model overlaps with Machel, 2000b. However, in contrast to the Neogene, Cretaceous normal seawater appears insufficient for syndepositional and early-burial near-surface island dolomitisation. Several factors may have hindered unmodified early-burial near-surface seawater dolomitisation during the Cretaceous compared to Late Cenozoic (e.g. dolomite saturation levels, Mg-budget, and Mg:Ca of dolomitising fluids; Arvidson and Mackenzie, 1997, 1999; Kaczmarek and Sibley, 2011; Al-Disi et al., 2019). Our proposed model may have overcome these primary kinetic barriers only through the previously discussed contributions from magmatism. Therefore, magmatism appears essential for extensive island dolomitisation by Cretaceous normal salinity seawater, rather than serving as an alternative as in Late Cenozoic islands (Machel, 2000b).

Cold deep seawater below calcite saturation depth (>1000 m;Flood and Chivas, 1995; James and Choquette, 1983; Saller, 1986) may not solely explain deep-seated island dolomites in various locations. We conducted an analysis using two main factors: (a) the current depths of Cretaceous islands and atolls (Wodejebato, Ita-Mai-Tai, Horizon, MIT, Allison, and Resolution), and (b) the age of the oldest pelagic cap on each atoll, to roughly estimate how long these drowned atolls stayed below 1000 mbsl. This calculation considered that pelagic caps accumulate at depths >200 mbsl (James and Jones, 2015) and assumed that the subsidence rates were constant. The analysis suggests that these islands were exposed to deep marine water below 1000 m for a prolonged period, ~20–56 Ma (Heezen et al., 1973; Winterer et al., 1973; Larson et al., 1995; Pearson, 1995; detailed calculations are available in Supplemental Sheet T13). However, dolomites were only seen to be associated with magmatic emplacements (e.g. Resolution and Allison guyots). Notably, deep Cenozoic samples from Hawaii (Saller and Winterbottom, 2022) and the Cenozoic Limalok atoll lacked dolomites (Ogg et al., 1995). Our study implies that magmatically driven hydrothermal dolomitisation through sill emplacement explains the depth of deep-seated dolomites in Resolution and potentially Allison guyots. This mechanism might also elucidate deep-seated dolomites in other atolls and islands during the Cretaceous and other periods with significant magmatism. For instance, in Xisha Islands, Miocene-Pliocene magmatism(s) were proposed to influence dolomitisation and dolomite transformation (Wei et al., 2006, 2008; Wang et al., 2018a; Li et al., 2023b; Liu et al., 2023) while other studies suggest normal to near-normal seawater dolomitisation without a significant impact from Miocene-Pliocene magmatism(s) (e.g. Bi et al., 2018; Wang et al., 2018b, 2022; Li et al., 2023a).

Our findings and the absence of early dolomites in other Cretaceous islands indicate that Cretaceous normal seawater alone might not suffice for widespread syndepositional and early-burial near-surface massive dolomitisation on various carbonate platforms. The Phanerozoic early near-surface dolomites dataset (Manche and Kaczmarek, 2021) shows that ≥70% of Cretaceous dolomites were formed in restricted depositional settings with elevated evaporation, temperature, and Mg:Ca. In contrast, Neogene dolomites are mainly associated with open-marine settings, indicative of normal seawater dolomitisation. This is reflected in our dataset where only few Cretaceous large isolated carbonate platforms were dolomitised by evaporated seawater (Malta, Adriatic, Apenninic, and Apulian platforms; Gatt, 2012; Read et al., 2016; Vinci et al., 2017; Torrieri et al., 2021; Supplemental Sheet T2). Hence, modification of Cretaceous seawater appears necessary. Some geochemical and petrographic characteristics of dolomites in our study and other examples of large-scale Cretaceous platform dolomitisation (e.g. mesohaline reflux dolomitisation of Zebbag Formation, Newport et al., 2017) highlight the need for cautious interpretation as they might overlap with near-surface early-burial and syndepositional normal (i.e. unmodified) seawater dolomites. Similarly, geochemistry and petrography of Derbyshire Platform's dolomites would reflect predominantly seawater origin with low dolomitisation temperature (<50 °C), while the new findings suggest influence of high volcanism heat and mixing with magmatic fluids (Breislin et al., 2020; Frazer et al., 2023). Therefore, comprehensive interpretation should consider additional factors like dolomite geometry, geological settings, and timing of dolomitisation (e.g. Budd, 1997).

6. Conclusion

This study provides insights into the formation of two rare examples of shallow-burial seawater-like Cretaceous island dolomitisation. Integrating geochemical observations, burial and thermal modelling of the limestone host rock, and core-log-seismic data indicates a magmatically driven hydrothermal dolomitisation origin. The magmatic emplacement facilitated dolomitisation by maintaining a high heat flow which would substantially increase the flux of circulating seawater and overcome the very limited dolomitisation potential and rate of Cretaceous seawater. The presence of Fe-rich dolomites suggests slight modification of the dolomitising seawater by mixing with the released H_2O–CO_2–SO_2–HCl-rich magmatic-hydrothermal fluids during upward flow. Acidic conditions might have facilitated leaching of metals (Mg and Fe) from basaltic basement and sills, resulting in enrichment of circulating dolomitising seawater. Our model might have overcome significant kinetic barriers such as low ambient temperature and Mg:Ca of seawater through magmatically associated vigorous heat flux and slight modification of seawater. Therefore, magmatically active Cretaceous islands had greater potentiality for seawater dolomitisation than passive counterparts. This mechanism may have broader applicability to other "island dolostones", particularly in explaining deep-seated post-depositional dolomites (e.g. Xisha Islands). It presents an alternative explanation to the interpretation of deep-seated dolomites, which is often attributed to dolomitisation by deep marine waters below calcite saturation depth. The absence of near-surface early-burial and syndepositional massive dolostones formed by unmodified seawater in any of the other Cretaceous islands and atolls implies reduced effectiveness of syndepositional and near-surface early-burial massive dolomitisation by Cretaceous normal (i.e. unmodified) seawater, questioning some of the previous interpretations. Therefore, we recommend that caution should be exercised in interpreting these dolomites as they may share certain characteristics with syndepositional and early-burial near-surface seawater dolomites, making it necessary to consider additional aspects (dolomite geometry, geological settings, and timing of dolomitisation).

CRediT authorship contribution statement

Mahmoud Samir El-Yamani: Conceptualization, Formal analysis, Funding acquisition, Investigation, Methodology, Resources, Project administration, Data curation, Visualization, Software, Writing – original draft, Writing-review & editing. **Cédric M. John:** Conceptualization, Methodology, Project administration, Supervision, Resources, Writing – review & editing. **Rebecca Bell:** Conceptualization, Methodology, Project administration, Supervision, Resources, Software, Writing – review & editing.

Declaration of competing interest

The authors declare that they have no known competing financial interests or personal relationships that could have appeared to influence the work reported in this paper.

Data availability

Data used in this research is open access data

Acknowledgment

The results presented here are part of Mahmoud Samir El-Yamani's PhD research at Imperial College London, funded by a full scholarship (MM21/19) from the Ministry of Higher Education and Scientific Research of Egypt under support from the Egyptian Bureau for Cultural and Educational Affairs. This study benefited from samples and data from the International Ocean Discovery Program (IODP) and its predecessors (ODP and DSDP). We thank Schlumberger, Ikon Science, and Lloyd's Register for providing access to Petrel®, RokDoc®, and Interactive Petrophysics® software, respectively. The authors would like to thank Carl Jaquemyn and Qi Adlan for helping in setting up the polarised light and cathodoluminescence microscopes. The Associate Editor Marco Brandano is thanked for the editorial handling and the constructive reviews that helped to improve the initial version of this paper. The authors thank the reviewers (Cathy Hollis and Luca Martire) for their thorough and constructive reviews and comments that helped to improve the initial version of this paper. David Budd is thanked for the useful discussion on the earlier versions of the manuscript.

Appendix A. Supplementary data

Supplementary data to this article can be found online at https://doi.org/10.1016/j.marpetgeo.2024.106741.

References

Aarnes, I., Podladchikov, Y., Svensen, H., 2012. Devolatilization-induced pressure build-up: implications for reaction front movement and breccia pipe formation. Geofluids 12 (4), 265–279.
Aharon, P., Socki, R.A., Chan, L., 1987. Dolomitization of atolls by sea water convection flow: test of a hypothesis at Niue, South Pacific. J. Geol. 95 (2), 187–203.
Al-Disi, Z.A., Bontognali, T.R., Jaoua, S., Attia, E., Al-Kuwari, H.A.S., Zouari, N., 2019. Influence of temperature, salinity and Mg^{2+}: Ca^{2+} ratio on microbially-mediated formation of Mg-rich carbonates by virgibacillus strains isolated from a sabkha environment. Sci. Rep. 9 (1), 1–12.
Andrié, C., Jean-Baptiste, P., Pierre, C., Déjardin, P., Fichez, R., Poupeau, J.J., Rougerie, F., 1998. Pore water geochemistry and mixing processes within the Tahiti barrier reef. Geochem. Cosmochim. Acta 62 (16), 2809–2822.
Arnaud, H.M., Flood, P.G., Strasser, A., 1995. Resolution guyot (hole 866A, mid-Pacific mountains): facies evolution and sequence stratigraphy: Northwest Pacific atolls and guyots. In: Proceedings of the Ocean Drilling Program. Scientific results, pp. 133–159, 143.
Arvidson, R.S., Mackenzie, F.T., 1997. Tentative kinetic model for dolomite precipitation rate and its application to dolomite distribution. Aquat. Geochem. 2, 273–298.
Arvidson, R.S., Mackenzie, F.T., 1999. The dolomite problem; control of precipitation kinetics by temperature and saturation state. Am. J. Sci. 299 (4), 257–288.
Arvidson, R.S., Guidry, M.W., Mackenzie, F.T., 2011. Dolomite controls on Phanerozoic seawater chemistry. Aquat. Geochem. 17, 735–747.
Bai, Y., Gui, Z., Li, M., Dong, D., Wu, S., Wang, Z., 2019. Crustal thickness over the NW Pacific and its tectonic implications. J. Asian Earth Sci. 185, 104050.
Baker, P.E., Castillo, P.R., Condliffe, E., 1995. Petrology and geochemistry of igneous rocks from allison and resolution guyots, sites 865 and 866: northwest pacific atolls and guyots. In: Proceedings of the Ocean Drilling Program. Scientific results, pp. 245–261, 143.
Baudin, F., Deconinck, J.F., Sachsenhofer, R.F., Strasser, A., Arnaud, H., 1995. 12. Organic geochemistry and clay mineralogy of lower cretaceous sediments from allison and resolution guyots (sites 865 and 866), mid-pacific mountains. Proceedings of the Ocean Drilling Program, Scientific Reports 143, 173–196.
Bell, B., Butcher, H., 2002. On the emplacement of sill complexes: evidence from the faroe–shetland basin. In: The North Atlantic Igneous Province: Stratigraphy, Tectonic, Volcanic and Magmatic Processes, 197. Geol. Soc. London. Spec. Publ., pp. 307–329
Benjakul, R., Hollis, C., Robertson, H.A., Sonnenthal, E.L., Whitaker, F.F., 2020. Understanding controls on hydrothermal dolomitisation: insights from 3D reactive transport modelling of geothermal convection. Solid Earth 11 (6), 2439–2461.
Bi, D.J., Zhai, S.K., Zhang, D.J., Liu, X.F., Liu, X.Y., Jiang, L.J., Zhang, A.B., 2018. Constraints of fluid inclusions and C, O isotopic compositions on the origin of the dolomites in the Xisha Islands, South China Sea. Chem. Geol. 493, 504–517.
Breislin, C., Crowley, S., Banks, V.J., Marshall, J.D., Millar, I.L., Riding, J.B., Hollis, C., 2020. Controls on dolomitization in extensional basins: an example from the Derbyshire Platform, UK. J. Sediment. Res. 90 (9), 1156–1174.
Brennan, S.T., Lowenstein, T.K., Cendón, D.I., 2013. The major-ion composition of Cenozoic seawater: the past 36 million years from fluid inclusions in marine halite. Am. J. Sci. 313 (8), 713–775.
Budd, D.A., 1997. Cenozoic dolomites of carbonate islands: their attributes and origin. Earth Sci. Rev. 42 (1–2), 1–47.
Carballo, J., Land, L.S., Miser, D.E., 1987. Holocene dolomitization of supratidal sediments by active tidal pumping, Sugarloaf Key, Florida. J. Sediment. Res. 57 (1), 153–165.
Carmichael, R.S., 1989. Practical Handbook of Physical Properties of Rocks and Minerals. CRC Press, Boca Raton, FL.
Caruso, S., Van Kranendonk, M.J., Baumgartner, R.J., Fiorentini, M.L., Forster, M.A., 2021. The role of magmatic fluids in the~ 3.48 Ga Dresser Caldera, Pilbara Craton: new insights from the geochemical investigation of hydrothermal alteration. Precambrian Res. 362, 106299.
Chatalov, G.A., 1971. Schemes for the size of textural elements in carbonate rocks. Rev. Bulg. Geol. Soc. 32, 374–377.
Chen, L., Chiang, H.T., Wu, J.N., Chiao, L.Y., Shyu, C.T., Liu, C.S., Chen, S.C., 2020. The focus thermal study around the spreading center of southwestern Okinawa trough. Tectonophysics 796, 228649.
Clague, D.A., Paduan, J.B., Dreyer, B.M., Chadwick Jr., W.W., Rubin, K.R., Perfit, M.R., Fundis, A.T., 2018. Chemical variations in the 1998, 2011, and 2015 lava flows from axial seamount, Juan de fuca ridge: cooling during ascent, lateral transport, and flow. G-cubed 19 (9), 2915–2933.
Collignon, M., Schmid, D.W., Galerne, C., Lupi, M., Mazzini, A., 2018. Modelling fluid flow in clastic eruptions: application to the Lusi mud eruption. Mar. Petrol. Geol. 90, 173–190.
Dasgupta, R., Jackson, M.G., Lee, C.T.A., 2010. Major element chemistry of ocean island basalts—conditions of mantle melting and heterogeneity of mantle source. Earth Planet Sci. Lett. 289 (3–4), 377–392.
Davies, R., Bell, B.R., Cartwright, J.A., Shoulders, S., 2002. Three-dimensional seismic imaging of Paleogene dike-fed submarine volcanoes from the northeast Atlantic margin. Geology 30 (3), 223–226.
Deer, W.A., Howie, R.A., Zussman, J., 1966. An Introduction to the Rock-Forming Minerals. Longman, London, p. 528.
Demicco, R.V., Lowenstein, T.K., Hardie, L.A., Spencer, R.J., 2005. Model of seawater composition for the Phanerozoic. Geology 33 (11), 877–880.
Dickson, J.A.D., Kenter, J.A.M., 2014. Diagenetic evolution of selected parasequences across a carbonate platform: late Paleozoic, Tengiz Reservoir, Kazakhstan. J. Sediment. Res. 84 (8), 664–693.
Division of Marine and Large Program. (n.d.). Scientific Ocean Drilling Programme wireline-logging Data. https://mlp.ldeo.columbia.edu/logdb/scientific_ocean_drilling/.
Drever, J.I., 1997. The Geochemistry of Natural Waters, Surface and Groundwater Environments. Prentice Hall), Englewood Cliffs, New Jersey, p. 436p.
El-Yamani, M.S., John, C.M., Bell, R., 2022. Stratigraphic evolution and karstification of a Cretaceous Mid-Pacific atoll (Resolution Guyot) resolved from core-log-seismic integration and comparison with modern and ancient analogues. Basin Res. 34 (5), 1536–1566.
Fairhurst, C., Brown, E.T., Detournay, E., Marsily, G.D., Nikolaevshiy, V., Pearson, J.R., et al., 1999. Underground Nuclear Testing in French Polynesia: Stability and Hydrology Issues.
Flood, P.G., 1998. Origin of white Sucrosic dolomite within shallow-water limestones, ODP hole 866A, resolution guyot, mid-Pacific mountains: Strontium isotopic evidence for the role of sea water in dolomitization. Reefs and Carbonate Platforms in the Pacific and Indian Oceans 137–144.
Flood, P.G., Chivas, A.R., 1995. Origin of massive dolomite, Leg 143, hole 866A, resolution guyot, mid-Pacific mountains: Northwest Pacific atolls and guyots. In: Proceedings of the Ocean Drilling Program. Scientific Results, pp. 161–169, 143.
Flood, P.G., Fagerstrom, J.A., Rougerie, F., 1996. Interpretation of the origin of massive replacive dolomite within atolls and submerged carbonate platforms: strontium isotopic signature ODP Hole 866A, Resolution Guyot, Mid-Pacific Mountains. Sediment. Geol. 101 (1–2), 9–13.
Flügel, E., 2010. Microfacies of Carbonate Rocks: Analysis, Interpretation and Application, vol. 976. springer, Berlin, p. 2004.
Frazer, M., Hollis, C., Whitaker, F., 2023. Dolomitisation of carbonate platform margins by fault-controlled geothermal convection: insights from coupling stratigraphic and reactive transport models. The Depositional Record 9 (3), 714–733.
Fritz, P., Smith, D.G.W., 1970. The isotopic composition of secondary dolomites. Geochem. Cosmochim. Acta 34 (11), 1161–1173.
Gabellone, T., Whitaker, F., 2016. Secular variations in seawater chemistry controlling dolomitization in shallow reflux systems: insights from reactive transport modelling. Sedimentology 63 (5), 1233–1259.
Gamo, T., Okamura, K., Charlou, J.L., Urabe, T., Auzende, J.M., Ishibashi, J., et al., 1997. Acidic and sulfate-rich hydrothermal fluids from the Manus back-arc basin, Papua New Guinea. Geology 25 (2), 139–142.
Gatt, P., 2012. Carbonate Facies, Depositional Sequences and Tectonostratigraphy of the Palaeogene Malta Platform (Doctoral Dissertation. Durham University.

Glover, P., 2000. Petrophysics MSc Course Notes. University of Leeds, UK.
Gregg, J.M., Sibley, D.F., 1984. Epigenetic dolomitization and the origin of xenotopic dolomite texture. J. Sediment. Res. 54 (3), 908–931.
Gregg, J.M., Bish, D.L., Kaczmarek, S.E., Machel, H.G., 2015. Mineralogy, nucleation and growth of dolomite in the laboratory and sedimentary environment: a review. Sedimentology 62 (6), 1749–1769.
Gudbrandsson, S., Wolff-Boenisch, D., Gislason, S.R., Oelkers, E.H., 2011. An experimental study of crystalline basalt dissolution from 2≤ pH≤ 11 and temperatures from 5 to 75 C. Geochem. Cosmochim. Acta 75 (19), 5496–5509.
Guille, G., 1996. The Atolls of Mururoa and Fangataufa (French Polynesia). I: Geology-Petrology-Hydrogeology from Volcano to Atoll. Musee oceanographique, Monaco.
Hansen, D.M., 2006. The morphology of intrusion-related vent structures and their implications for constraining the timing of intrusive events along the NE Atlantic margin. J. Geol. Soc. 163 (5), 789–800.
Hardie, L.A., 1996. Secular variation in seawater chemistry: An explanation for the coupled secular variation in the mineralogies of marine limestones and potash evaporites over the past 600 my. Geology 24 (3), 279–283.
Heezen, B.C., MacGregor, I.D., Foreman, H.P., Forristall, G., Hekel, H., Hesse, R., Hoskins, R.H., Jones, E.J.W., Kaneps, A., Krasheninnikov, V.A., Ruef, M.H., 1973. Teritiary Pelagic Ooze on Ita-Mai-Tai Seamount, Equatorial Pacific: DSDP Site 200 and 201, vol. 20. Initial Reports of the Deep-Sea Drilling Project, pp. 87–96.
Heiken, G., 1972. Morphology and petrography of volcanic ashes. Geol. Soc. Am. Bull. 83 (7), 1961–1988.
Heinrich, C.A., Candela, P.A., 2014. Fluids and ore formation in the Earth's crust. In: Treatise on Geochemistry, second ed.) (Vol. 13. Elsevier, pp. 1–28.
Hemley, J.J., Cygan, G.L., Fein, J.B., Robinson, G.R., d'Angelo, W.M., 1992. Hydrothermal ore-forming processes in the light of studies in rock-buffered systems; I, Iron-copper-zinc-lead sulfide solubility relations. Econ. Geol. 87 (1), 1–22.
Henry, P., Guy, C., Cattin, R., Dudoignon, P., Sornein, J.F., Caristan, Y., 1996. A convective model of water flow in Mururoa basalts. Geochem. Cosmochim. Acta 60 (12), 2087–2109.
Hirani, J., Bastesen, E., Boyce, A., Corlett, H., Gawthorpe, R., Hollis, C., Whitaker, F., 2018. Controls on the formation of stratabound dolostone bodies, Hammam Faraun fault block, Gulf of Suez. Sedimentology 65 (6), 1973–2002.
Horita, J., 2014. Oxygen and carbon isotope fractionation in the system dolomite–water–CO2 to elevated temperatures. Geochem. Cosmochim. Acta 129, 111–124.
Horita, J., Zimmermann, H., Holland, H.D., 2002. Chemical evolution of seawater during the Phanerozoic: implications from the record of marine evaporites. Geochem. Cosmochim. Acta 66 (21), 3733–3756.
Huang, X., Betzler, C., Wu, S., Bernhardt, A., Eagles, G., Han, X., Hovland, M., 2020. First documentation of seismic stratigraphy and depositional signatures of Zhongsha atoll (Macclesfield Bank), South China Sea. Mar. Petrol. Geol. 117, 104349.
Huuse, M., Jackson, C.A.L., Van Rensbergen, P., Davies, R.J., Flemings, P.B., Dixon, R.J., 2010. Subsurface sediment remobilization and fluid flow in sedimentary basins: an overview. Basin Res. 22 (4), 342–360.
Infante-Paez, L., Marfurt, K.J., 2018. In-context interpretation: Avoiding pitfalls in misidentification of igneous bodies in seismic data. Interpretation 6 (4), SL29–SL42.
Iyer, K., Schmid, D.W., Planke, S., Millett, J., 2017. Modelling hydrothermal venting in volcanic sedimentary basins: impact on hydrocarbon maturation and paleoclimate. Earth Planet Sci. Lett. 467, 30–42.
Jacquemyn, C., El Desouky, H., Hunt, D., Casini, G., Swennen, R., 2014. Dolomitization of the Latemar platform: fluid flow and dolomite evolution. Mar. Petrol. Geol. 55, 43–67.
James, N.P., Choquette, P.W., 1983. Diagenesis 6. Limestones—the sea floor diagenetic environment. Geoscience Canada.
James, N.P., Jones, B., 2015. Origin of Carbonate Sedimentary Rocks. John Wiley & Sons.
Jamtveit, B., Svensen, H., Podladchikov, Y.Y., Planke, S., 2004. Hydrothermal vent complexes associated with sill intrusions in sedimentary basins. Geol. Soc. Lond., Spec. Publ. 234, 233–241.
Jean-Baptiste, P., Leclerc, A.M., 2000. Self-limiting geothermal convection in marine carbonate platforms. Geophys. Res. Lett. 27 (6), 743–746.
Jenkyns, H.C., 1995. Carbon-isotope stratigraphy and paleoceanographic significance of the lower Cretaceous shallow-water carbonates of resolution guyot, mid-Pacific mountains. Proceedings of the Ocean Drilling Program, Scientific Reports 143, 99–104.
Jenkyns, H.C., Paull, C.K., Cummins, D.I., Fullagar, P.D., 1995. Strontium-isotope stratigraphy of lower Cretaceous atoll carbonates in the mid-Pacific mountains. Proceedings of the Ocean Drilling Program, Scientific Reports 143, 89–97.
Jones, B., 1989. Calcite rafts, peloids, and micrite in cave deposits from Cayman Brae, British West Indies. Can. J. Earth Sci. 26 (4), 654–664.
Jones, B., 2005. Dolomite crystal architecture: genetic implications for the origin of the Tertiary dolostones of the Cayman Islands. J. Sediment. Res. 75 (2), 177–189.
Jones, B., Luth, R.W., 2002. Dolostones from Grand Cayman, British west Indies. J. Sediment. Res. 72 (4), 559–569.
Jones, B., Luth, R.W., MacNEIL, A.J., 2001. Powder X-ray diffraction analysis of homogeneous and heterogeneous sedimentary dolostones. J. Sediment. Res. 71 (5), 790–799.
Jones, G., Whitaker, F., Smart, P., Sanford, W., 2000. Numerical modelling of geothermal and reflux circulation in Enewetak Atoll: implications for dolomitization. J. Geochem. Explor. 69, 71–75.
Judd, A., Hovland, M., 2007. Seabed Fluid Flow: the Impact on Geology, Biology and the Marine Environment. Cambridge University Press, p. 475pp.
Kaczmarek, S.E., Sibley, D.F., 2011. On the evolution of dolomite stoichiometry and cation order during high-temperature synthesis experiments: an alternative model for the geochemical evolution of natural dolomites. Sediment. Geol. 240 (1–2), 30–40.
Keizer, P., Koppers, A., Staudigel, H., Helly, J., 2001. The seamount Catalog in EarthRef. Org. In: AGU Fall Meeting Abstracts. OS11B-0358, 2001.
Kenter, J.A.M., Harris, P.M., Collins, J.F., Weber, L.J., Kuanysheva, G., Fischer, D.J., 2006. Late Visean to Bashkirian platform cyclicity in the central Tengiz buildup, Precaspian Basin, Kazakhstan: depositional evolution and reservoir development. In: Harris, P.M., Weber, L.J. (Eds.), Giant Hydrocarbon Reservoirs of the World: from Rocks to Reservoir Characterization and Modeling: AAPG Memoir 88. SEPM Special Publication, pp. 7–54.
Kenter, J.A., Ivanov, M., 1995. 18. Parameters controlling acoustic properties OF carbonate and volcaniclastic sediments at sites 866 and 8691. In: Proceedings of the Ocean Drilling Program. Scientific Reports, pp. 287–303, 143.
Koeshidayatullah, A., Corlett, H., Stacey, J., Swart, P.K., Boyce, A., Robertson, H., et al., 2020. Evaluating new fault-controlled hydrothermal dolomitization models: insights from the Cambrian dolomite, western Canadian sedimentary basin. Sedimentology 67 (6), 2945–2973.
Kohout, F.A., Henry, H.R., Banks, J.E., Smith, K.L., Griffin, G.M., 1977. Hydrogeology related to geothermal conditions of the Floridan Plateau. The geothermal nature of the Floridan Plateau 21, 1–41.
Kurnosov, V.B., Zolotarev, B.P., Artamonov, A.V., 2007. Sea water-basalt interaction in the Pacific seamounts: low-temperature environments. Water-Rock Interaction-Proceedings of the 12th International Symposium on Water-Rock Interaction WRI-12, 135–138.
Kurnosov, V., Zolotarev, B., Eroshchev-Shak, V., Artamonov, A., Kashinzev, G., 1995. Alteration of basalts from the West Pacific guyots, Legs 143 and 144. Proc. Ocean Drill. Progr. Sci. Results 144, 475–491.
Land, L.S., 1973. Contemporaneous dolomitization of Middle Pleistocene reefs by meteoric water, north Jamaica. Bull. Mar. Sci. 23, 64–90.
Land, L.S., 1985. The origin of massive dolomite. J. Geol. Educ. 33 (2), 112–125.
Land, L.S., 1991. Dolomitization of the Hope Gate Formation (north Jamaica) by seawater: reassessment of mixing-zone dolomite. In: Taylor, H.P., O'Neil, J.R., Kaplan, I.R. (Eds.), Stable Isotope Geochemistry: a Tribute to Samuel Epstein, vol. 3. Geochem. Soc. Spec. Publ., pp. 121–133
Larson, R.L., Erba, E., Nakanishi, M., Bergersen, D.D., Lincoln, J.M., 1995. Stratigraphic, vertical subsidence, and paleolatitude histories of Leg 144 guyots. In: Proceedings of the Ocean Drilling Program. Scientific results, pp. 915–933, 144.
Leclerc, A.M., Jean-Baptiste, P., Texier, D., Broc, D., 1999. Density-induced water circulations in atoll coral reefs: a numerical study. Limnol. Oceanogr. 44 (5), 1268–1281.
Lee, Y.I., Friedman, G.M., 1987. Deep-burial dolomitization in the Ordovician Ellenburger Group carbonates, west Texas and southeastern New Mexico. J. Sediment. Res. 57 (3), 544–557.
Leroy, S., Lucazeau, F., d'Acremont, E., Watremez, L., Autin, J., Rouzo, S., et al., 2010. Contrasted styles of rifting in the eastern Gulf of Aden: a combined wide-angle, multichannel seismic, and heat flow survey. G-cubed 11 (7).
Li, R., Jones, B., Qiao, P., Cui, Y., Pei, J., Liu, X., Shao, L., 2023. Genesis of island dolostones during rapid island subsidence: example from the Xisha (Paracel) islands, South China Sea. Sedimentology 70 (6), 1785–1811.
Li, X., Shi, Z., Han, L., Hu, X., 2023. Geochemical characteristics of hydrogen, oxygen, carbon isotopes and REE of cenozoic dolomites in Well Xike 1, Xisha Islands, South China sea and the significance for dolomitization in island-reef areas. Front. Earth Sci. 10, 1064808.
Liu, G., Wu, S., Gao, J., Zhang, H., Han, X., Qin, Y., et al., 2023. Seismic architecture of Yongle isolated carbonate platform in Xisha Archipelago, South China sea. Front. Earth Sci. 11, 1100675.
Lucia, F.J., 1995. Rock-fabric/petrophysical classification of carbonate pore space for reservoir characterization. AAPG Bull. 79 (9), 1275–1300.
Machel, H.G., 1999. Effects of groundwater flow on mineral diagenesis, with emphasis on carbonate aquifers. Hydrogeol. J. 7, 94–107.
Machel, H.G., 2000. Application of cathodoluminescence to carbonate diagenesis. In: Cathodoluminescence in Geosciences. Springer Berlin Heidelberg, Berlin, Heidelberg, pp. 271–301.
Machel, H.G., 2000. Dolomite formation in Caribbean Islands: driven by plate tectonics? J. Sediment. Res. 70 (5), 977–984.
Machel, H.G., Burton, E.A., 1994. Golden Grove dolomite, Barbados; origin from modified seawater. J. Sediment. Res. 64 (4a), 741–751.
Machel, H.G., Lonnee, J., 2002. Hydrothermal dolomite—a product of poor definition and imagination. Sediment. Geol. 152 (3–4), 163–171.
Machel, H.G., Burton, E.A., 1991. Factors governing cathodoluminescence in calcite and dolomite, and their implications for studies of carbonate diagenesis. In: Barker, C.E., Kopp, O.C. (Eds.), Luminescence Microscopy and Spectroscopy–Qualitative and Quantitative Applications. SEPM (Society for Sedimentary Geology) Short Course, pp. 37–57, 25.
MacNeil, A., Jones, B., 2003. Dolomitization of the Pedro Castle formation (Pliocene), Cayman brac, British west Indies. Sediment. Geol. 162 (3–4), 219–238.
Magee, C., Maharaj, S.M., Wrona, T., Jackson, C.A.L., 2015. Controls on the expression of igneous intrusions in seismic reflection data. Geosphere 11 (4), 1024–1041.
Manche, C.J., Kaczmarek, S.E., 2019. Evaluating reflux dolomitization using a novel high-resolution record of dolomite stoichiometry: a case study from the Cretaceous of central Texas, USA. Geology 47 (6), 586–590.
Manche, C.J., Kaczmarek, S.E., 2021. A global study of dolomite stoichiometry and cation ordering through the Phanerozoic. J. Sediment. Res. 91 (5), 520–546.
Manton, B., Müller, P., Mazzini, A., Zastrozhnov, D., Jerram, D.A., Millett, J.M., et al., 2022. Characterizing ancient and modern hydrothermal venting systems. Mar. Geol. 447, 106781.

Marine Geoscience Data System. (n.d.). RNDB10WT 1988 Seismic Reflection Data Processing Steps by the Institute for Geophysics at the University of Texas (UTIG). https://www.marine-geo.org/collections/#!/collection/Seismic.
Matthews, A., Katz, A., 1977. Oxygen isotope fractionation during the dolomitization of calcium carbonate. Geochem. Cosmochim. Acta 41 (10), 1431–1438.
Mazzullo, S.J., 1992. Geochemical and neomorphic alteration of dolomite: a review. Carbonates Evaporites 7, 21–37.
McArthur, J.M., Howarth, R.J., Shields, G.A., 2012. Strontium isotope stratigraphy, Chapter 7, 127–144. In: Gradstein, F.M., Ogg, J.G., Schmitz, M.D., Ogg, G.M. (Eds.), A Geologic Time Scale. Elsevier B.V, p. 1144, 1(2).
Melim, L.A., Westphal, H., Swart, P.K., Eberli, G.P., Munnecke, A., 2002. Questioning carbonate diagenetic paradigms: evidence from the Neogene of the Bahamas. Mar. Geol. 185 (1–2), 27–53.
Mills, J.V., Gomes, M.L., Kristall, B., Sageman, B.B., Jacobson, A.D., Hurtgen, M.T., 2017. Massive volcanism, evaporite deposition, and the chemical evolution of the Early Cretaceous Ocean. Geology 45 (5), 475–478.
Mitchum Jr., R.M., Vail, P.R., Thompson III, S., 1977. Seismic stratigraphy and global changes of sea level; Part 2, the depositional sequence as a basic unit for stratigraphic analysis. In: Payton, C.E. (Ed.), Seismic Stratigraphy; Applications to Hydrocarbon Exploration, vol. 26. AAPG Memoir, pp. 53–62.
Montaggioni, L.F., Braithwaite, C.J.R., 2009. Chapter Seven reef Hydrogeology. Developments in Marine Geology 5, 271–321.
Müller, I.A., Rodriguez-Blanco, J.D., Storck, J.C., do Nascimento, G.S., Bontognali, T.R., Vasconcelos, C., et al., 2019. Calibration of the oxygen and clumped isotope thermometers for (proto-) dolomite based on synthetic and natural carbonates. Chem. Geol. 525, 1–17.
Murdmaa, I., Kurnosov, V., Vasilyeva, V., 1995. Clay mineralogy of the shallow-water deposits on Allison and Resolution guyots, sites 865 and 866. Proc. Ocean Drill. Progr. Sci. Results (Vol. 144,, 459–468.
Newport, R., Hollis, C., Bodin, S., Redfern, J., 2017. Examining the interplay of climate and low amplitude sea-level change on the distribution and volume of massive dolomitization: Zebbag Formation, Cretaceous, Southern Tunisia. The Depositional Record 3 (1), 38–59.
Newport, R., Segura, M., Redfern, J., Hollis, C., 2020. The interaction of tectonics, climate and eustasy in controlling dolomitization: A case study of Cenomanian–Turonian, shallow marine carbonates of the Iberian Basin. Sedimentology 67 (5), 2223–2247.
Niyazi, Y., Warne, M., Ierodiaconou, D., 2021. Post-rift magmatism and hydrothermal activity in the central offshore Otway Basin and implications for igneous plumbing systems. Mar. Geol. 438, 106538.
Northrop, D.A., Clayton, R.N., 1966. Oxygen-isotope fractionations in systems containing dolomite. J. Geol. 74 (2), 174–196.
ODP Initial Reports, 1993. Shipboard Scientific Party Core Description of Site 866. http://www-odp.tamu.edu/publications/143_IR/VOLUME/CHAPTERS/cor_0866.pdf.
ODP Initial Reports, 1993. Shipboard Scientific Party Core Description of Site 865. http://www-odp.tamu.edu/publications/143_IR/VOLUME/CHAPTERS/cor_0865.pdf.
Ogg, J.G., 1993. Geomagnetic polarity time scale. http://www-odp.tamu.edu/publications/143_IR/VOLUME/CHAPTERS/cor_0865.pdf.
Ogg, J.G., Camoin, G.F., Arnaud Vanneau, A., 1995. Limalok Guyot: depositional history of the carbonate platform from downhole logs at Site 871 (lagoon). In: Proceedings-Ocean Drilling Program Scientific Results. National Science Foundation, pp. 233–254.
Omosanya, K.O., Eruteya, O.E., Siregar, E.S., Zieba, K.J., Johansen, S.E., Alves, T.M., Waldmann, N.D., 2018. Three-dimensional (3-D) seismic imaging of conduits and radial faults associated with hydrothermal vent complexes (Vøring Basin, Offshore Norway). Mar. Geol. 399, 115–134.
O'Neil, J.R., Epstein, S., 1966. Oxygen isotope fractionation in the system dolomite-calcite-carbon dioxide. Science 152 (3719), 198–201.
Pal, M., Taberner, C., Tueckmantel, C., 2015. Simulation of end-member scenarios of density-driven flow: prediction of dolostone geobody dimensions using COMSOL. Geological Society, London, Special Publications 406 (1), 209–228.
Parfitt, L., Wilson, L., 2009. Fundamentals of Physical Volcanology. John Wiley & Sons.
Paull, C.K., Fullagar, P.D., Bralower, T.J., Rohl, U., 1995. Seawater ventilation of mid-Pacific guyots drilled during Leg 143. the Proceedings ofthe Ocean Drilling Program 143, 231–241. Initial Reports.
Paytan, A., Kastner, M., Campbell, D., Thiemens, M.H., 2004. Seawater sulfur isotope fluctuations in the Cretaceous. science 304 (5677), 1663–1665.
Pearson, P.N., 1995. Planktonic foraminifer biostratigraphy and the development of pelagic caps on guyots in the Marshall Islands Group. In: Rack, F., McNutt, M.K. (Eds.), Proceeding of the Ocean Drilling Program J. Haggerty, I. Premoli Silva, Scientific Results, vol. 144, pp. 21–59.
Pearson-Grant, S.C., Miller, C.A., Carson, L.B., Bertrand, E.A., Leonard, G.S., 2022. Influences on geothermal circulation in the Okataina volcanic centre, New Zealand. J. Volcanol. Geoth. Res. 432, 107705.
Planke, S., Rasmussen, T., Rey, S.S., Myklebust, R., 2005. Seismic characteristics and distribution of volcanic intrusions and hydrothermal vent complexes in the Vøring and Møre basins. In: Geological Society, London, Petroleum Geology Conference Series of. Geological Society of London, pp. 833–844, 6.
Planke, S., Symonds, P.A., Alvestad, E., Skogseid, J., 2000. Seismic volcanostratigraphy of large-volume basaltic extrusive complexes on rifted margins. J. Geophys. Res. Solid Earth 105 (B8), 19335–19351.
Pleydell, S.M., Jones, B., Longstaffe, F.J., Baadsgaard, H., 1990. Dolomitization of the oligocene–miocene bluff formation on Grand Cayman, British west Indies. Can. J. Earth Sci. 27 (8), 1098–1110.
Pockalny, R., Barth, G., Eakins, B., Kelley, K.A., Wertman, C., 2021. Multiple melt source origin of the line islands (Pacific Ocean). Geology 49 (11), 1358–1362.
Pringle, M.S., Duncan, R.A., 1995. Radiometric ages of basaltic lavas recovered at Sites 865, 866, and 869: Northwest Pacific atolls and guyots. In: Proceedings of the Ocean Drilling Program. Scientific results, pp. 277–283, 143.
Read, J.F., Husinec, A., Cangialosi, M., Loehn, C.W., Prtoljan, B., 2016. Climate controlled, fabric destructive, reflux dolomitization and stabilization via marine-and synorogenic mixed fluids: an example from a large Mesozoic, calcite-sea platform, Croatia. Palaeogeogr. Palaeoclimatol. Palaeoecol. 449, 108–126.
Ren, M., Jones, B., 2016. Diagenesis in limestone-dolostone successions after 1 million years of rapid sea-level fluctuations: a case study from Grand Cayman, British West Indies. Sediment. Geol. 342, 15–30.
Ren, M., Jones, B., 2017. Spatial variations in the stoichiometry and geochemistry of Miocene dolomite from Grand Cayman: implications for the origin of island dolostone. Sediment. Geol. 348, 69–93.
Ren, M., Jones, B., 2018. Genesis of island dolostones. Sedimentology 65 (6), 2003–2033.
JOIDES. Resolution Science Operator (n.d.). International Ocean Discovery Program, Ocean Drilling Data of ODP Leg 143. https://web.iodp.tamu.edu/OVERVIEW/?&exp=143.
Rivers, J.M., 2023. Warm acidified seawater: a dolomite solution. J. Sediment. Res. 93 (3), 187–201.
Rivers, J.M., Yousif, R., Kaczmarek, S.E., Al-Shaikh, I., 2021. Cenozoic coastal carbonate deposits of Qatar: evidence for dolomite preservation bias in highly-arid systems. Sedimentology 68 (2), 771–787.
Robertson, H., Corlett, H., Hollis, C., Kibblewhite, T., Whitaker, F., 2019. Listwanitization as a Source of Mg for Dolomitization: Field Evaluation in Atlin, British Columbia. Barcelona, Goldschmidt Conference. August 2019.
Roelofse, C., Alves, T.M., Kamal'deen, O.O., 2021. Reutilisation of hydrothermal vent complexes for focused fluid flow on continental margins (Modgunn Arch, Norwegian Sea). Basin Res. 33 (2), 1111–1134.
Röhl, U., Strasser, A., 1995. Diagenetic alterations and geochemical trends in early Cretaceous shallow-water limestones of Allison and resolution guyots (sites 865 to 868). In: Proceedings of the Ocean Drilling Program. Scientific results, pp. 197–229, 143.
Rougerie, F., Wauthy, B., 1993. The endo-upwelling concept: from geothermal convection to reef construction. Coral Reefs 12 (1), 19–30.
Ryan, B.H., Kaczmarek, S.E., Rivers, J.M., 2020. Early and pervasive dolomitization by near-normal marine fluids: new lessons from an Eocene evaporative setting in Qatar. Sedimentology 67 (6), 2917–2944.
Sager, W.W., 1995. Structural implications of gravity anomalies, resolution and Heezen guyots, mid-Pacific mountains: Northwest Pacific atolls and guyots. In: Proceedings of the Ocean Drilling Program, vol. 143. Scientific Reports, pp. 419–429.
Sager, W.W., Winterer, E.L., Firth, J.V., Arnaud, H., Baker, P.A., Baudin, F., Bralower, T. J., Castillo, P., Cooper, P., Flood, P.G., Golovchenko, X., Iryu, Y., Ivanov, M., Jenkyns, H.C., Kenter, J.A.M., Murdmaa, I., Mutterlose, J., Nogi, Y., Paull, C.K., Polgreen, E., Rohl, U., Sliter, W.V., Strasser, A., Swinburne, N.H.M., Tarduno, J.A., van Waasbergen, R., 1993. Site 866. Proceedings of the Ocean Drilling Program 143, 181–271. Initial Reports.
Sager, W.W., Winterer, E.L., Firth, J.V., Arnaud, H., Baker, P.A., Baudin, F., Bralower, T. J., Castillo, P., Cooper, P., Flood, P.G., Golovchenko, X., Iryu, Y., Ivanov, M., Jenkyns, H.C., Kenter, J.A.M., Murdmaa, I., Mutterlose, J., Nogi, Y., Paull, C.K., Polgreen, E., Rohl, U., Sliter, W.V., Strasser, A., Swinburne, N.H.M., Tarduno, J.A., van Waasbergen, R., 1993. Site 865. Proceedings of the Ocean Drilling Program 143, 111–180. Initial Reports.
Sahlström, F., Jonsson, E., Högdahl, K., Troll, V.R., Harris, C., Jolis, E.M., Weis, F., 2019. Interaction between high-temperature magmatic fluids and limestone explains 'Bastnäs-type'REE deposits in central Sweden. Sci. Rep. 9 (1), 15203.
Saller, A.H., 1984. Petrologic and geochemical constraints on the origin of subsurface dolomite, Enewetak Atoll: an example of dolomitization by normal seawater. Geology 12 (4), 217–220.
Saller, A.H., 1986. Radiaxial calcite in lower Miocene strata, subsurface Enewetak Atoll. J. Sediment. Res. 56 (6), 743–762.
Saller, A.H., Lounsbury, K., Birchard, M., 2001. Facies control on dolomitization and porosity in the Devonian Swan Hills Formation in the Rosevear area, west-central Alberta. Bull. Can. Petrol. Geol. 49 (4), 458–471.
Saller, A., Winterbottom, C., 2022. Deep marine diagenesis, offshore Hawaii and Enewetak, with implications to older carbonates. The Depositional Record. Special Issue: Carbonate Diagenesis: a celebration of the work of J.A.D. (Tony) Dickson 9 (3), 526–572.
Schlanger, S.O., Graf, D.L., Goldsmith, J.R., 1963. Subsurface Geology of Eniwetok Atoll. Geological Survey Professional. US Government Printing Office. Paper 260-BB, Washington, DC, p. 76.
Scotese, C.R., Wright, N., 2018. PALEOMAP paleodigital elevation models (PaleoDEMS) for the Phanerozoic PALEOMAP Project. Earth byte. https://www.earthbyte.org/paleodem-resource-scotese-and-wright-2018.
Seewald, J.S., Reeves, E.P., Bach, W., Saccocia, P.J., Craddock, P.R., Shanks III, W.C., et al., 2015. Submarine venting of magmatic volatiles in the eastern Manus Basin, Papua New Guinea. Geochem. Cosmochim. Acta 163, 178–199.
Shalev, N., Bontognali, T.R., Wheat, C.G., Vance, D., 2019. New isotope constraints on the Mg oceanic budget point to cryptic modern dolomite formation. Nat. Commun. 10 (1), 5646.
Shea, J.J., Ezad, I.S., Foley, S.F., Lanati, A.W., 2022. The Eastern Australian Volcanic Province, its primitive melts, constraints on melt sources and the influence of mantle metasomatism. Earth Sci. Rev., 104168
Sheppard, S.M., Schwarcz, H.P., 1970. Fractionation of carbon and oxygen isotopes and magnesium between coexisting metamorphic calcite and dolomite. Contrib. Mineral. Petrol. 26, 161–198.

Sibley, D.F., 1990. Unstable to stable transformations during dolomitization. J. Geol. 98 (5), 739–748.
Sibley, D.F., Gregg, J.M., 1987. Classification of dolomite rock textures. J.Sediment. Geol. 57, 967–975.
Sigurdsson, H., Leckie, R.M., Acton, G.D., Miller, C.M., Maddox, E.M., 1997. Caribbean volcanism, Cretaceous/Tertiary impact, and ocean climate history: synthesis of Leg 165. Proc. Ocean Drill. Progr. Initial Rep. 165, 377–400.
Skogseid, J., Pedersen, T., Eldholm, O., Larsen, B.T., 1992. Tectonism and magmatism during NE Atlantic continental break-up: the Vøring Margin. Geological Society, London, Special Publications 68 (1), 305–320.
Śliwiński, M.G., Whalen, M.T., Meyer, F.J., Majs, F., 2012. Constraining clastic input controls on magnetic susceptibility and trace element anomalies during the Late Devonian punctata Event in the Western Canada Sedimentary Basin. Terra. Nova 24 (4), 301–309.
Staudigel, H., Park, K.H., Pringle, M., Rubenstone, J.L., Smith, W.H.F., Zindler, A., 1991. The longevity of the South Pacific isotopic and thermal anomaly. Earth Planet Sci. Lett. 102 (1), 24–44.
Stein, C.A., Stein, S., 1992. A model for the global variation in oceanic depth and heat flow with lithospheric age. Nature 359 (6391), 123–129.
Steinmann, M., Déjardin, P., 2004. The temporal evolution of fluid flow through the Tahiti barrier reef traced by Sr isotopes and pore water chemistry. Chem. Geol. 203 (1–2), 51–73.
Steuber, T., Rauch, M., 2005. Evolution of the Mg/Ca ratio of Cretaceous seawater: implications from the composition of biological low-Mg calcite. Mar. Geol. 217 (3–4), 199–213.
Stoessell, R.K., Coke, J.G., Easley, D.H., 2002. Localized thermal anomalies in haloclines of coastal Yucatan sinkholes. Ground Water 40 (4), 416–424.
Stranghoener, M., Schippers, A., Dultz, S., Behrens, H., 2018. Experimental microbial alteration and Fe mobilization from basaltic rocks of the ICDP HSDP2 drill core, Hilo, Hawaii. Front. Microbiol. 9, 1252.
Strasser, A., Arnaud, H., Baudin, F., Röhl, U., 1995. Small-scale shallow-water carbonate sequences of resolution guyot (sites 866, 867, and 868). In: Proceedings of the Ocean Drilling Program. scientific results, pp. 119–131, 143.
Suzuki, Y., Iryu, Y., Inagaki, S., Yamada, T., Aizawa, S., Budd, D.A., 2006. Origin of atoll dolomites distinguished by geochemistry and crystal chemistry: Kita-daito-jima, northern Philippine Sea. Sediment. Geol. 183 (3–4), 181–202.
Swart, P.K., Melim, L.A., 2000. The origin of dolomites in Tertiary sediments from the margin of Great Bahama Bank. J. Sediment. Res. 70 (3), 738–748.
Swartz, J.H., 1958. Geothermal Measurements on Eniwetok and Bikini Atolls. U.S. Geological Survey, Professional Paper, 260-U, pp. 711–741.
Szabó, N.P., Kilik, R., Dobróka, M., 2023. Robust reservoir identification by multi-well cluster analysis of wireline logging data. Heliyon 9 (5), E15957.
Tarduno, J.A., Sager, W.W., Nogi, Y., 1995. Early cretaceous magnetostratigraphy and paleolatitudes from the mid-pacific mountains: preliminary results bearing on guyot formation and pacific plate translation. Proc. Ocean Drill. Progr. Sci. Results 143, 395–398.
Timofeeff, M.N., Lowenstein, T.K., Da Silva, M.A.M., Harris, N.B., 2006. Secular variation in the major-ion chemistry of seawater: evidence from fluid inclusions in Cretaceous halites. Geochem. Cosmochim. Acta 70 (8), 1977–1994.
Torrieri, S., Volery, C., Bazalgette, L., Strauss, C.G., 2021. From outcrop to subsurface model—large-scale fractured zones in Apulian platform carbonates (Maiella Mountains, Central Apennines, Italy). AAPG (Am. Assoc. Pet. Geol.) Bull. 105 (12), 2449–2476.
Turcotte, D.L., Schubert, G., 2002. Geodynamics, second ed. Wiley, New York, p. 848pp.
Vahrenkamp, V.C., Swart, P.K., 1994. Late Cenozoic dolomites of the Bahamas: metastable analogues for the genesis of ancient platform dolomites. Dolomites: A volume in honour of Dolomieu 133–153.
Valdes, P.J., Scotese, C.R., Lunt, D.J., 2021. Deep ocean temperatures through time. Clim. Past Discuss 1483–1506.
Vallier, T.L., Jefferson, W.S., 1981. Volcanogenic sediments from Hess Rise and the mid-Pacific mountains, deep sea drilling Project Leg 62 J. Thiede. Proceedings of the Initial Reports of the Deep Sea Drilling Project 62, 545–557.
Vasconcelos, C., McKenzie, J.A., Warthmann, R., Bernasconi, S.M., 2005. Calibration of the $\delta^{18}O$ paleothermometer for dolomite precipitated in microbial cultures and natural environments. Geology 33 (4), 317–320.
Veizer, J., 1983. Chemical diagenesis in carbonates: Theory and application of trace element technique. In: Arthur, M.A., Anderson, T.J. (Eds.), Stable Isotopes in Sedimentary Geology: Society of Economic Paleontologists and Mineralogists Short Course, 10, pp. 3–100.
Vinci, F., Iannace, A., Parente, M., Pirmez, C., Torrieri, S., Giorgioni, M., 2017. Early dolomitization in the lower Cretaceous shallow-water carbonates of Southern Apennines (Italy): Clues about palaeoclimatic fluctuations in western Tethys. Sediment. Geol. 362, 17–36.
Wang, G., Li, P., Hao, F., Zou, H., Yu, X., 2015. Dolomitization process and its implications for porosity development in dolostones: a case study from the lower Triassic Feixianguan formation, Jiannan area, eastern Sichuan basin, China. J. Petrol. Sci. Eng. 131, 184–199.
Wang, H., Zhao, Q., Wu, S., Wang, D., Wang, B., 2018. Post-rifting magmatism and the drowned reefs in the Xisha Archipelago domain. J. Ocean Univ. China 17, 195–208.
Wang, L., Shi, X., Ren, Z., Pei, J., Yang, X., Shen, Y., et al., 2020. Tectono-thermal evolution features of the reef body developing area in the Liyue Basin, Southern South China Sea. Chin. J. Geophys. 63 (8), 3050–3062.
Wang, R., Jones, B., Yu, K., 2019. Island dolostones: genesis by time-transgressive or event dolomitization. Sediment. Geol. 390, 15–30.
Wang, J., Wu, S., Kong, X., Ma, B., Li, W., Wang, D., Gao, J., Chen, W., 2018. Subsurface fluid flow at an active cold seep area in the Qiongdongnan Basin, northern South China Sea. Journal of Asian Earth Sciences 168, 17–26.
Wang, R., Xiao, Y., Yu, K., Jones, B., Wu, L., Liang, F., et al., 2022. Temperature regimes during formation of Miocene island dolostones as determined by clumped isotope thermometry: Xisha Islands, South China Sea. Sediment. Geol. 429, 106079.
Wang, R., Yu, K., Jones, B., Wang, Y., Zhao, J., Feng, Y., et al., 2018. Evolution and development of miocene “island dolostones” on Xisha islands, South China sea. Mar. Geol. 406, 142–158.
Warren, J., 2000. Dolomite: occurrence, evolution, and economically important associations. Earth Sci. Rev. 52 (1–3), 1–81.
Watson, D., Schofield, N., Jolley, D., Archer, S., Finlay, A.J., Mark, N., Hardman, J., Watton, T., 2017. Stratigraphic overview of palaeogene tuffs in the faroe–shetland basin, NE atlantic margin. J. Geol. Soc. 174 (4), 627–645.
Wei, X., Jia, C.Z., Meng, W.G., 2008. Dolomitization characteristics of carbonate rock in Xisha Islands and its formation: a case study of Well Xichen-1. J. Jilin Univ. (Earth Sci. Ed.) 38 (2), 217–224.
Wei, X., Zhu, Y., Xu, H., Zhao, G., Li, Y., 2006. Discussion on Neogene dolostone forming condition in Xisha Islands: evidences from isotope C and O and fluid inclosures. Acta Petrol. Sin. 22 (9), 2394–2404.
Wheeler, C.W., Aharon, P., Ferrell, R.E., 1999. Successions of late Cenozoic platform dolomites distinguished by texture, geochemistry, and crystal chemistry; Niue, South Pacific. J. Sediment. Res. 69 (1), 239–255.
Whitaker, F.F., Xiao, Y., 2010. Reactive transport modeling of early burial dolomitization of carbonate platforms by geothermal convection. AAPG Bull. 94 (6), 889–917.
Whitaker, F.F., Smart, P.L., Vahrenkamp, V.C., Nicholson, H., Wogelius, R.A., 1994. Dolomitization by near-normal seawater? Field evidence from the Bahamas. Dolomites: A Volume in Honour of Dolomieu 109–132.
Wilckens, F.K., Reeves, E.P., Bach, W., Seewald, J.S., Kasemann, S.A., 2019. Application of B, Mg, Li, and Sr isotopes in acid-sulfate vent fluids and volcanic rocks as tracers for fluid-rock interaction in back-arc hydrothermal systems. G-cubed 20 (12), 5849–5866.
Wilson, A.M., Sanford, W., Whitaker, F., Smart, P., 2001. Spatial patterns of diagenesis during geothermal circulation in carbonate platforms. Am. J. Sci. 301 (8), 727–752.
Wilson, E.N., Hardie, L.A., Phillips, O.M., 1990. Dolomitization front geometry, fluid flow patterns, and the origin of massive dolomite: the Triassic Latemar buildup, northern Italy. Am. J. Sci. 290 (7), 741–796.
Winterer, E.L., Ewing, J.I., Douglas, R.G., Jarrard, R.D., Lancelot, Y., Moberly, R.M., Moore Jr., T.C., Peter, H.R., Schlanger, S.O., 1973. Site 171. Initial Rep. Deep Sea Drill. Proj. 17, 283–334.
Winterer, E.L., Sager, W.W., 1995. 31. Synthesis of drilling results from the mid-pacific mountains: regional context and IMPLICATIONS1. Proc. Ocean Drill. Progr. Sci. Results 143, 497–535.
Woronick, R.E., Land, L.S., 1985. Late burial diagenesis, lower cretaceous pearsall and lower glen rose formations, South Texas. In: Schneiderman, N., Harris, P.M. (Eds.), Carbonate Cements. Soc. Econ. Paleontol. Mineral., Spec, vol. 36. . Publ., pp. 265–275
Zenger, D.H., 1968. Determination of calcite and dolomite composition using the air comparison pycnometer. J. Sediment. Petrol. 38, 373–377.
Zhao, H., Jones, B., 2012. Genesis of fabric-destructive dolostones: a case study of the brac formation (oligocene), cayman brac, British west indies. Sediment. Geol. 267, 36–54.
Zhao, H., Jones, B., 2012. Origin of “island dolostones”: a case study from the cayman formation (miocene), cayman brac, British west indies. Sediment. Geol. 243, 191–206.
Zhou, J., Poulsen, C.J., Pollard, D., White, T.S., 2008. Simulation of modern and middle Cretaceous marine $\delta^{18}O$ with an ocean-atmosphere general circulation model. Paleoceanography 23 (3).